

Rare-earth silicide thin films on the Si(111) surface

S. Sanna,* C. Dues, and W. G. Schmidt

Department Physik, Universität Paderborn, 33095 Paderborn, Germany

F. Timmer and J. Wollschläger

Department Physik, Universität Osnabrück, 49069 Osnabrück, Germany

M. Franz, S. Appelfeller, and M. Dähne

Institut für Festkörperphysik, Technische Universität Berlin, 10623 Berlin, Germany

(Received 6 January 2016; revised manuscript received 18 April 2016; published 6 May 2016)

Rare-earth induced layered structures on the Si(111) surface are investigated by a combined approach consisting of *ab initio* thermodynamics, electron and x-ray diffraction experiments, angle-resolved photoelectron spectroscopy, and scanning tunneling microscopy. Our density functional theory calculations predict the occurrence of structures with different periodicity, depending on the rare-earth availability. Microscopic structural models are assigned to the different silicide phases on the basis of stability criteria. The thermodynamically stable theoretical models are then employed to interpret the experimental results. The agreement between the simulated and measured scanning tunneling microscopy images validates the proposed structural models. The electronic properties of the surfaces are discussed on the basis of the calculated electronic band structure and photoelectron spectroscopy data.

DOI: [10.1103/PhysRevB.93.195407](https://doi.org/10.1103/PhysRevB.93.195407)**I. INTRODUCTION**

Metallic rare-earth silicides can be grown epitaxially as few-monolayers thin films on the Si(111) substrate by rare-earth deposition and thermal treatment [1–3]. The resulting metal/semiconductor interface is characterized by an extraordinarily low Schottky-barrier height of 0.3–0.4 eV on *n*-type substrates. Due to the marginal lattice mismatch [4] between substrate and thin film, the interface is furthermore characterized by a low defect concentration and a high stability. Because of these characteristics, the rare-earth silicides on *n*-type silicon are considered ideal candidates for Ohmic contacts [5,6]. The relatively high barrier height on *p*-type substrates makes them interesting for infrared detectors and photovoltaic applications, instead [7]. For submonolayer coverage, a variety of structures with different periodicities was found [8–12]. Furthermore, the rare-earth silicides are the basis for the self-organized formation of nanowires on several Si substrates with other orientations [13–19].

Despite the large and growing interest on silicide thin films on Si(111), our knowledge of these systems is still fragmentary. A multitude of surface reconstructions or nanostructures with different periodicities has been observed, depending on the rare earth species and rare-earth coverage [8–12,18,20–25]. Unfortunately, not all the silicide structures appear in both microscopy and diffraction experiments, which hinders the investigations. The observed structures are characterized by different stoichiometries and heights. For Dy, e.g., a full monolayer results in a film with 1×1 periodicity and DySi₂ hexagonal structure, multilayer silicides grow in a film with $\sqrt{3} \times \sqrt{3}$ periodicity and Dy₃Si₅ composition, while submonolayer coverage results in structures with $2\sqrt{3} \times 2\sqrt{3}$ or 5×2 periodicity [10].

Structural models have been proposed for some of the silicide layers on the basis of scanning tunneling microscopy images (STM) [10] and low-energy electron diffraction data (LEED). However, no first-principles calculations at the atomic scale that can confirm or reject the proposed models have been performed for most structures up to date. In general, our theoretical knowledge of the two-dimensional rare-earth silicides is largely incomplete and limited to the simplest Y and Er silicide structures [21,24–29]. To the best of our knowledge, no theoretical investigations of the silicide structures in the submonolayer range are available in the literature.

The aim of the present paper is therefore to provide a comprehensive overview on the rare-earth silicide films observed by microscopy or electron diffraction, characterize them, and propose a corresponding microscopic model. To this end, we combine *ab initio* thermodynamics with surface sensitive experimental techniques such as LEED, STM, surface x-ray diffraction (SXRD), and angle-resolved photoelectron spectroscopy (ARPES). A phase diagram showing the stable silicide phase depending on the rare-earth availability is calculated. The phase diagram shows that a multitude of structures with different periodicity and stoichiometry can be formed at given thermodynamic conditions. The structural models of the stable phases are discussed in detail and employed to compute simulated STM images within the Tersoff-Hamann approximation. The simulated STM images are then used to interpret the corresponding experimental data. Moreover, the calculated band structures of the stable surface terminations are compared with ARPES measurements, in order to assign the measured bands to the corresponding electronic states. For the sake of clarity, we reproduce here some experimental data from Refs. [12,20] concerning the silicide phases with 5×2 and 1×1 periodicity. Calculations are performed using Dy (atomic number 66) as a prototypical trivalent rare earth. Additional calculations are performed for silicides formed by Y, Tb, and Er as further trivalent rare earths (atomic numbers

*simone.sanna@uni-paderborn.de

39, 65, and 68, respectively). This allows for a comparison between the different rare-earth ions and to outline chemical trends, e.g., related to the lanthanide contraction.

The paper is structured as follows. Section II describes the theoretical foundations of the *ab initio* thermodynamics and the computational details of the calculations. The sample preparation and characterization together with the experimental details are given in Sec. III. In Sec. IV, we present and discuss the results of this combined investigation for each examined film structure. Finally, Sec. V summarizes the main results of this work.

II. THEORY

A. Methodology

Total-energy density functional theory (DFT) calculations are performed within the generalized gradient approximation [30] (GGA) in the Perdew-Burke-Ernzerhof formulation [31] as implemented in the Vienna *ab initio* simulation package (VASP) [32,33]. In order to test the dependence of our results on the exchange and correlation functional, additional calculations within the local density approximation (LDA) have been performed, whenever the total energy difference of commensurate slabs modeling competing structures with the same stoichiometry was smaller than 60 meV. Projector augmented wave [34,35] (PAW) potentials with projectors up to $l = 1$ for H, $l = 2$ for Si, and $l = 3$ for Y and for the rare-earth atoms as well as a plane-wave cutoff of 400 eV have been used. As no other valence state than RE^{3+} has been observed for the rare-earth ions in the silicide structures, we constrain the valence state of the investigated rare-earth ions treating $n - 1$ f electrons as core states. This approach, commonly referred to as frozen-core method, allows for a proper treatment of the lanthanides within DFT [36–38]. Thereby a number of 4 ($3s^2 3p^2$), 11 ($4s^2 4p^6 5s^2, 4d^1$), and 9 ($5d^1 5p^6 6s^2$) valence electrons is considered for Si, Y, and the other rare-earth atoms, respectively.

Bulk rare-earth silicides crystallize in several phases with hexagonal, tetragonal, or orthorhombic structures and RESi_{2-x} stoichiometry ($-0.1 \leq x \leq 0.5$), where RE stands for rare earth. The occurring structure depends on the nature of the rare earth, the value of x , and the temperature [40,41]. Because of their almost perfect lattice match, only hexagonal stoichiometric RESi_2 phases with AIB_2 structure (space group D_{3d}^3) are considered in this work [41]. The total energies of RESi_2 bulk silicides in the hexagonal phase have been calculated using primitive cells consisting of three atoms and optimizing the respective lattice constants within Γ -centered $8 \times 8 \times 4$ k -point meshes [42]. The considered elemental rare earths crystallize above room temperature in a metallic hexagonal close-packed structure (space group D_{6h}^4) [41]. They are modeled by unit cells consisting of two atoms and Γ -centered $12 \times 12 \times 12$ k -point meshes [42]. This approach allows to reproduce the lattice parameters within 2% of the measured values. The calculated lattice parameters are listed in Table I along with the experimental values for comparison. The gas phase of hydrogen—used for saturation of Si dangling bonds at the bottom slab side—has been modeled by a dimer in a vacuum box of sides $10 \times 11 \times 12 \text{ \AA}^3$. No correction for

TABLE I. Calculated and measured [39] lattice parameters of silicon in the diamond structure and of the elemental rare earths in the hcp phase. All values are in angstroms.

System	a_{DFT}	c_{DFT}	$a_{\text{exp.}}$	$c_{\text{exp.}}$
Si	5.468	—	5.431	—
Er	3.587	5.559	3.559	5.585
Dy	3.621	5.622	3.590	5.648
Tb	3.632	5.671	3.601	5.694
Y	3.656	5.666	3.647	5.730

the known GGA overbinding problem is considered [43], as it would not qualitatively change the conclusions of this work.

The silicide surfaces are modeled with slabs of different size. The slabs consist of six Si bilayers stacked along the [111] crystallographic direction to model the substrate, the silicide thin film of variable structure and height, and a vacuum region of at least 15 Å. The dangling bonds at the lower face of the slabs are saturated by hydrogen atoms. The atomic positions are relaxed until the residual Hellmann-Feynman forces are lower than 0.001 eV/Å. Thereby the whole silicide layer and three Si bilayers are free to relax, while three Si bilayers and the hydrogen atoms are kept constrained in order to model the substrate. Test calculations show that adding further substrate layers does not result in noticeable changes on calculated geometries and band structures. Dipole-correction algorithms have been used to correct the spurious interactions of the slabs with their periodic images [44,45]. The computational details of the slab calculations for silicide phases of different periodicity are summarized in Table II.

The effective mass tensor is estimated in harmonic approximation [46,47] as

$$\left(\frac{1}{m^*}\right)_{ij} = \frac{m_e}{\hbar^2} \left(\frac{\partial^2 \varepsilon(k)}{\partial k_i \partial k_j}\right). \quad (1)$$

In this equation, m_e is the mass of the free electron, \hbar the reduced Planck constant, and $\varepsilon(k)$ are the Kohn-Sham electronic states, which are fitted in the ij direction to estimate the effective mass of electrons (highest occupied state) or holes (lowest unoccupied state).

Simulated constant-current STM images are calculated within the Tersoff-Hamann model [48,49] on the basis of partial densities of states (LDOS). A careful interpretation of the calculated images is necessary, as tip effects—which are neglected within this approach—can play an important role in the STM imaging process [50]. Nonetheless, this

TABLE II. Computational parameters employed to model silicide structures of different periodicity. n_{RE} labels the number of rare-earth atoms and n_{tot} the total number of atoms per unit cell. The rare-earth coverage (in monolayers) is given by θ .

Periodicity	n_{RE}	θ	n_{tot}	k points
1×1	1	1	16	$12 \times 12 \times 1$
$\sqrt{3} \times \sqrt{3}$	6	2	56	$12 \times 12 \times 1$
$2\sqrt{3} \times 2\sqrt{3}$	6	0.5	162	$6 \times 6 \times 1$
5×2	2–8	0.2–0.8	134–157	$6 \times 6 \times 1$

method often provides a fairly good qualitative prediction of the experimental observations.

B. Thermodynamic framework

The experimentally observed silicide films on the Si(111) surface are characterized by a different rare-earth content, i.e., by a different stoichiometry. In order to compare the formation energy of silicide films with different composition, we use the thermodynamic grand-canonical potential (or Landau potential) Ω , approximated as [51,52]

$$\Omega(\mu_{\text{Si}}, \mu_{\text{RE}}) \approx E^{\text{DFT}}(N_{\text{Si}}, N_{\text{RE}}) - \sum_i^{\text{Si,RE}} \mu_i N_i. \quad (2)$$

In this equation, $E^{\text{DFT}}(N_{\text{Si}}, N_{\text{RE}})$ is the DFT total energy of a slab containing N_{Si} silicon atoms and N_{RE} rare-earth atoms. μ_{Si} and μ_{RE} are the corresponding chemical potentials and represent the experimental growth conditions. The sum in Eq. (2) also extends to the H atoms employed to saturate the Si dangling bonds at the bottom side of the slabs.

As the free energy of the film structures ($F = U - TS$, with U being the internal energy) should be used rather than the DFT total energy, Eq. (2) represents an approximation. However, this approximation is valid as long as the contribution of the film formation entropy S to its energy at a given temperature is similar for the different silicide films. Furthermore, considering that the influence of the pressure variation on the film energy can be neglected, and that one expects a compensation of the effects of the zero point vibrations on the total energy and on the chemical potentials, the total energy E is usually replaced by the DFT total energy E^{DFT} in explicit calculations [51].

The Landau potential Ω is expressed as a function of the chemical potentials μ_{Si} and μ_{RE} , which are the variables in Eq. (2). However, the thermodynamically allowed range for these variables is constrained by several conditions. The upper limits are given by the bulk phases:

$$\mu_i \leq \mu_i^{\text{bulk}} \quad i = \text{Si, RE}. \quad (3)$$

Furthermore the silicide films are in equilibrium with the Si substrate, which represents an infinite reservoir of Si atoms. This pins the value of μ_{Si} to $\mu_{\text{Si}}^{\text{bulk}}$ and allows to express the Landau potential as $\Omega = \Omega(\mu_{\text{RE}})$. The RE chemical potential can be controlled experimentally with the amount of rare earth deposited on the Si substrate before annealing.

If we restrict our investigation to silicide phases with a given stoichiometry $\text{RE}_\alpha\text{Si}_\beta$, the lower limit of μ_{RE} is given by

$$\alpha \mu_{\text{Si}}^{\text{bulk}} + \beta \mu_{\text{RE}} = \mu_{\text{Si}_\alpha\text{RE}_\beta}^{\text{bulk}} \quad (4)$$

whereby we use $\mu_{\text{Si}} = \mu_{\text{Si}}^{\text{bulk}}$ as we consider Si rich conditions. However, we also consider lower values of μ_{RE} , representing nonstoichiometric silicides with dilute rare-earth concentrations.

The values of the bulk chemical potentials are estimated by the total energy per formula unit calculated within DFT as described in Sec. II A. The corresponding values are compiled in Table III.

TABLE III. Chemical potentials (total energy per formula unit) of the bulk phases of relevant compounds (in eV).

System	μ	System	μ
ErSi ₂	-16.804	Er	-4.564
DySi ₂	-16.948	Dy	-4.533
TbSi ₂	-17.029	Tb	-4.556
YSi ₂	-18.877	Y	-6.433
Si	-5.424	H	-3.387

III. EXPERIMENT

Si(111) 7×7 substrates were prepared by repeated flashing of Si(111) wafers followed by slow cooling down in order to enable the formation of a defect free surface reconstruction. The silicide films were grown in situ by depositing rare-earth films on the clean Si(111) 7×7 surface held at room temperature followed by annealing to form the silicide. The base pressure was lower than 5×10^{-11} mbar and did not exceed 5×10^{-10} mbar during preparation. rare-earth exposures were determined using a quartz crystal microbalance with an absolute accuracy of $\pm 20\%$. One rare-earth monolayer is defined using the density of Si atoms at the unreconstructed Si(111) surface, $7.83 \times 10^{14} \text{ cm}^{-2}$. Annealing temperatures were controlled by an infrared pyrometer with an accuracy of about $\pm 20^\circ\text{C}$. As an exception, the Dy silicide films analyzed by spot profile analysis low-energy electron diffraction (SPA-LEED) and by surface x-ray diffraction (SXRD) were grown by rare-earth deposition at 450°C .

The STM experiments were performed in constant-current mode using a noncommercial instrument at a pressure of 5×10^{-11} mbar. The tunneling tips were prepared by electrochemical etching of tungsten wires and subsequent annealing within the STM chamber.

In-situ SXRD experiments were performed at the undulator beamline ID03 of the European Synchrotron Radiation Facility (ESRF, Grenoble, France) using the respective in-situ ultra high vacuum (UHV) setup and diffractometer in z -axis mode with a fixed incidence angle of 1° and a x-ray photon energy of 18 keV. In-plane and out-of-plane diffraction data were collected with an area detector. The measured data were background corrected to compare them with the structure factor calculated from the models developed here.

For the ARPES experiments, we used a chamber system equipped with a toroidal electron energy analyzer, allowing to measure sets of equal-energy maps in full k_{\parallel} space as well as standard dispersion curves along one azimuthal direction. The ARPES experiments were performed at the BUS beamline (U125/2-SGM) at BESSY II in Berlin using a photon energy of 41 eV.

Low-energy electron diffraction (LEED) experiments were performed to control the surface structure data. Additional experiments were performed in a different UHV chamber by means of a high-resolution LEED system to perform spot profile analysis (SPA-) LEED experiments.

IV. RESULTS

A plethora of rare-earth induced surface terminations is observed at the Si(111) surface, depending on the rare-earth

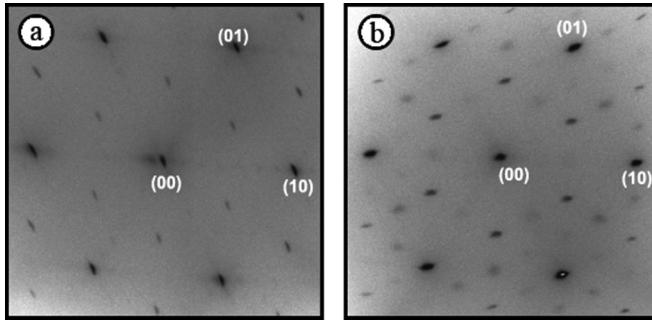


FIG. 1. SPA-LEED patterns of the rare earth (in this case Dy) deposited Si(111) surface revealing the formation of (a) a multilayer superstructure with $\sqrt{3} \times \sqrt{3}$ periodicity at high rare-earth coverage and (b) a superstructure with $2\sqrt{3} \times 2\sqrt{3}$ periodicity in the submonolayer region. The main diffraction spots are indexed according to the values of h and k .

coverage and on the thermal treatment. These structures are characterized by a variable rare-earth content, indicated by their chemical composition RESi_x . Three main growth regimes can be identified, depending on the rare-earth exposure. Around monolayer coverage, silicides with 1×1 periodicity and a stoichiometric composition with $x = 2$ are formed. Multilayer structures such as the phase with $\sqrt{3} \times \sqrt{3}$ periodicity and RE_3Si_5 composition are observed for higher rare-earth coverage. In the submonolayer region, different structures are observed (e.g., the $2\sqrt{3} \times 2\sqrt{3}$ or the 5×2 phase). In Fig. 1, we show exemplarily the SPA-LEED patterns of the Dy deposited Si(111) surface in the multilayer [Fig. 1(a)] and the submonolayer regime [Fig. 1(b)]. The diffraction spots reveal the formation of superstructures with $\sqrt{3} \times \sqrt{3}$ and $2\sqrt{3} \times 2\sqrt{3}$ periodicity, respectively. In the submonolayer region, a formal composition of the silicide films is difficult to define, as the Si/silicide interface is not abrupt, and the number of included Si substrate layers can be arbitrarily selected. Considering the thin films as the structure formed on top of a nonreconstructed Si(111) substrate, the $2\sqrt{3} \times 2\sqrt{3}$ structure has a nominal composition RE_6 and the 5×2 structure RESi_6 , as will be shown further below.

We start our investigation with the pristine, unreconstructed Si(111) surface and the adsorption of isolated rare-earth atoms on it. Then silicide monolayers, multilayers, and submonolayers are presented and analyzed. Finally, the relative stability of the surface reconstructions depending on the rare-earth coverage is discussed.

A. The Si(111) 1×1 surface

The basis for all the following investigation is the Si(111) surface. This surface is known to show a 2×1 LEED pattern if cleaved at room temperature or a 1×1 pattern if cleaved at temperatures below 20 K. After annealing at 400°C , a superstructure with a long-ranging 7×7 periodicity appears [53]. However, the presence of the deposited rare-earth adsorbates often prevents the formation of these surface reconstructions. Thus the nonreconstructed Si(111) surface is relevant in this work. Within our models, it is characterized by a hexagonal cell with a lattice constant of $a = 3.866 \text{ \AA}$,

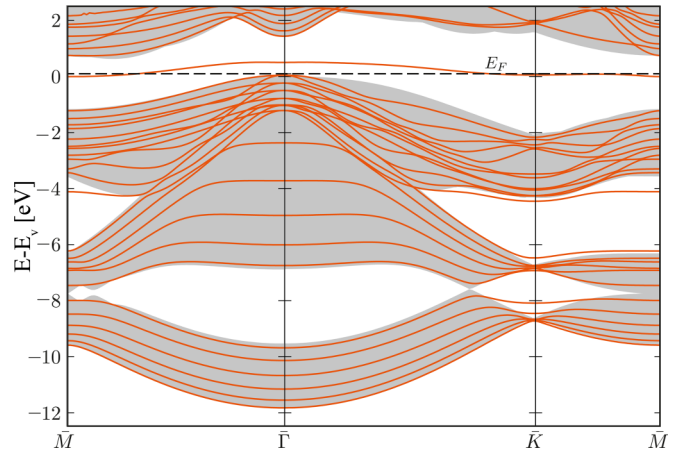


FIG. 2. Calculated band structure of the nonreconstructed Si(111) surface (orange bands). The localized state in the fundamental gap (in orange) is due to the surface dangling bonds. Projected Si bulk bands are shown in grey.

in good agreement with measured values. Cutting bulk Si perpendicularly to the $[111]$ crystallographic directions results in broken sp^3 bonds at the topmost Si layer, creating one dangling bond per surface unit cell. Indeed, the corresponding surface band structure with projected bulk states (displayed in Fig. 2) shows a single surface state localized within the electronic band gap. As the electronic orbitals of the topmost Si atoms have reduced orbital overlap, the corresponding surface states lower their energy less than bulk valence states and thus rise from the valence band into the electronic gap. The band is half-filled and crosses the Fermi level. The calculated electronic gap of about 0.67 eV is slightly smaller than the measured value, which is due to the underestimation of the band gaps in DFT calculations [51].

During the growth process, rare-earth ions are deposited at the Si(111) surface. In order to identify the energetically favorable adsorption sites, we have calculated the potential energy surface for the adsorption of isolated atoms at the Si(111) 1×1 surface. It is calculated constraining the lateral coordinates of the rare-earth atom and allowing its height as well as the remaining degrees of freedom of the uppermost three Si substrate bilayers to relax. We have evaluated the system energy for 56 lateral positions on a rectangular grid (average spacing 0.5 \AA). The energy between the grid points is then evaluated by bicubic interpolation of the calculated data. The outcome of our calculation in the case of Dy is shown in Fig. 3. The rare-earth ion avoids positions right on top of the topmost Si atoms or on bridge positions on the line joining them. It rather prefers an adsorption above the second Si layer atoms (hcp site, global minimum) or above the third Si-layer atoms (fcc site, local minimum). The latter two positions are typically addressed to as T_4 and H_3 , respectively [21]. The energy difference between the two sites amounts to 225 meV , and the low energy barrier between the two minima (about 300 meV) indicates a relatively high mobility of the adsorbates. The potential energy surface calculated for other rare earths (Tb and Er) strongly resemble Fig. 3, are characterized by very similar energy values, and are thus not shown in this work. Our results are consistent with previous semiempirical

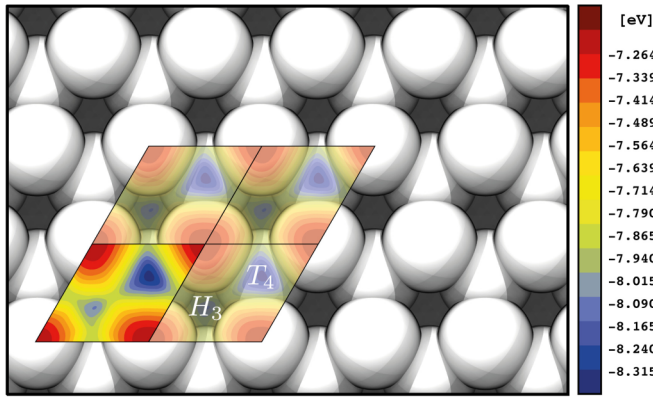


FIG. 3. Potential energy surface for the adsorption of a single Dy atom at the Si(111) surface. Blue regions indicate favorable adsorption sites.

tight-binding like calculations, which identified the hcp site as the favorable adsorption site of Er at the Si(111) surface on the basis of the resulting band structure of an ErSi₂ monolayer [21].

B. The RESi₂ monolayer with 1 × 1 periodicity

The deposition of a complete silicide monolayer on the Si(111) surface results in regular films with RESi₂ stoichiometry and 1 × 1 periodicity [1]. The model proposed by Stauffer *et al.* for the ErSi₂ monolayer describes the microscopic structure of most rare earth silicide monolayers at the Si(111) surface [21], including DySi₂ [23], HoSi₂ [22], GdSi₂ [24], and YSi₂ [24,29,54]. X-ray diffraction experiments confirmed the suggestion by Stauffer *et al.* for ErSi₂ [55]. According to this commonly accepted model, the surface termination consists of a hexagonal rare-earth monolayer underneath a buckled Si top layer [see Fig. 4(a)]. Thereby the rare-earth atoms lay above the Si(111) hcp site (at the T₄ position in Fig. 3), and the orientation

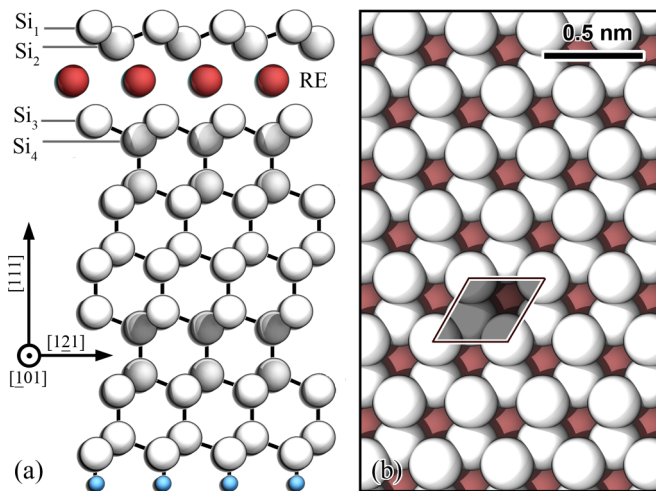


FIG. 4. Side view (a) and top view (b) of the rare-earth silicide monolayer with 1 × 1 periodicity on the Si(111) surface. Silicon atoms are shown in white and rare earth atoms in red. Hydrogen atoms saturating the Si dangling bonds at the bottom side of the slab are shown in light blue. The 1 × 1 surface unit cell is highlighted.

TABLE IV. Calculated distances (in angstroms) between atomic layers in the silicide structure with 1 × 1 periodicity in dependence of the rare earth. See Fig. 4 for atomic labels and definitions. In brackets, the corresponding distances calculated for bulk silicides are given together with the deviation in percents. For comparison, the bilayer distance within bulk Si amounts to 0.78 Å.

	Y	Tb	Dy	Er	Exp. [57]
Si ₁ -Si ₂	0.80	0.79	0.80	0.82	0.78
Si ₂ RE	1.89	1.90	1.88	1.85	1.90
	(1.98)–4.7	(1.98)–4.3	(1.97)–4.7	(1.94)–4.9	
RE-Si ₃	2.04	2.05	2.03	2.00	2.12
	(1.98)–3.1	(1.98)–3.3	(1.97)–2.3	(1.94)–3.0	
Si ₃ -Si ₄	0.91	0.91	0.91	0.92	0.83
Si ₂ -Si ₃	3.93	3.95	3.91	3.84	4.02
	(3.96)–0.8	(3.97)–0.5	(3.94)–0.8	(3.88)–0.9	

of the buckled Si top layer is opposite to that of the Si(111) substrate double layers.¹ The structure of the silicide film strongly resembles the silicide bulk phase with A1B₂ crystal structure, while the silicide layer grows on the Si substrate with the relationship Si(111) || RESi₂(0001). The presence of silicon vacancies in this structure has been ruled out by both Auger electron diffraction and STM measurements [10,12,56]. Our calculations confirm this model for all investigated silicides, DySi₂, TbSi₂, and ErSi₂.

A structural model in which the topmost Si layer has the same orientation as in the bulk bilayers is characterized by an higher formation energy by 0.187, 0.200, and 0.221 eV per 1 × 1 unit cell than the model in Fig. 4 for Tb, Dy, and Er, respectively. This is of the same order of magnitude as in previous calculations for the YSi₂ silicide monolayer [24,29,54]. Interestingly, the orientation of the uppermost bilayer can be switched by H adsorption [57]. A monolayer geometry based on the rare earth adsorbed at the local fcc minimum (or H₃ position, see Fig. 3) yields a locally stable configuration as well. However, this structure is 0.758, 0.761, and 0.760 eV per 1 × 1 unit cell less stable than the configuration shown in Fig. 4 for Tb, Dy, and Er, respectively.

Although all the investigated rare-earth silicide monolayers crystallize within the model in Fig. 4, the distances between atomic layers depend slightly on the rare-earth atom. The predicted distances for atomic layers labeled Si₁ to Si₄ in Fig. 4(a) are compiled in Table IV, together with experimental results for comparison [57]. The calculated data are in good agreement with the measured values obtained from surface extended x-ray absorption fine structure (SEXAFS) experiments. The interatomic distances between layers Si₂ and Si₃, i.e., the layers neighboring the rare-earth atoms, decrease with increasing atomic number of the rare earth. This behavior is expected, as the atomic radii of the rare-earth ions decrease with the atomic number (lanthanide contraction). Moreover, it can be noticed that the distances between the atomic layers in the silicide thin films are very close to the corresponding distances in free-standing bulk silicides. The largest deviation occurs for the Si₂-Er distance and amounts to 5%. Thus the

¹This behavior is currently referred to as *B orientation*.

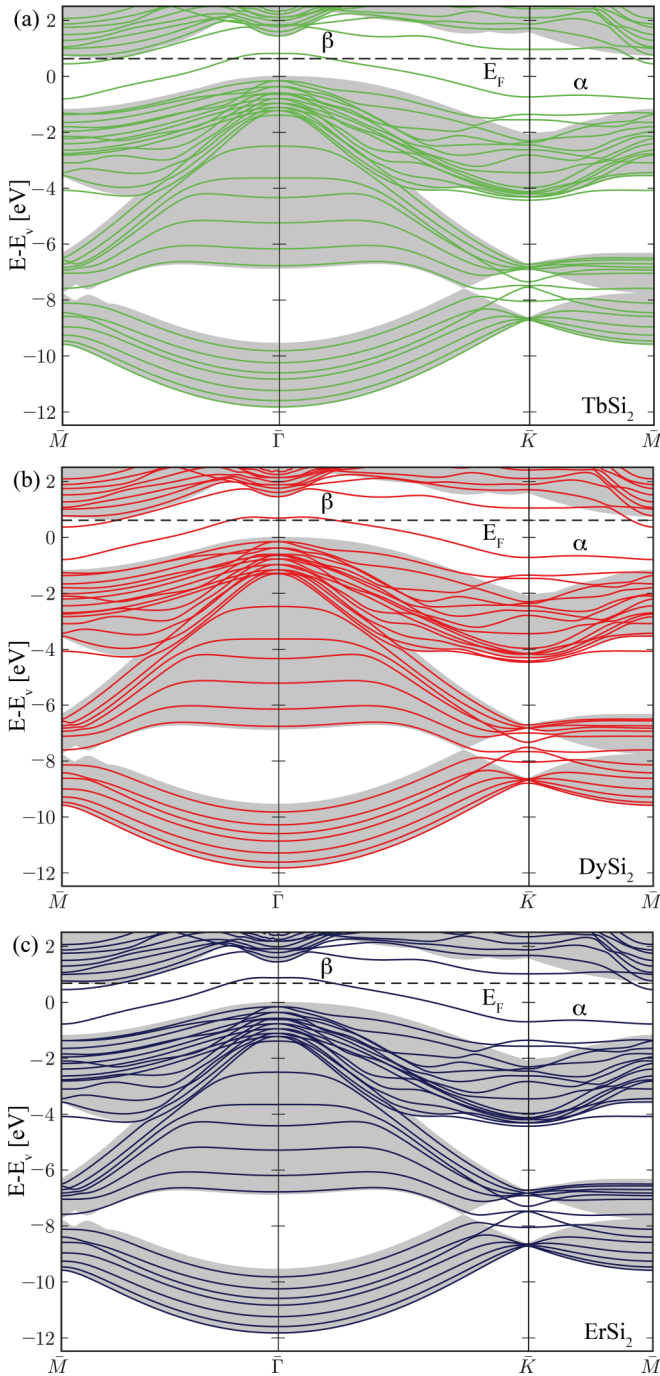


FIG. 5. Calculated band structures of the rare earth monolayer silicides on the Si(111) surface with 1×1 periodicity. (a) TbSi_2 , (b) DySi_2 , and (c) ErSi_2 . The localized states α and β in the fundamental gap are discussed in the text. Projected bulk bands are shown in grey.

grown silicide films with 1×1 periodicity are relatively well matched with the substrate, which explains the low defect density observed experimentally.

The electronic band structure calculated for the silicide slab model in Fig. 4 is shown in Fig. 5. The calculated band structure strongly resembles the projected bulk Si band structure (in grey). The main difference is represented by the prominent surface localized gap states that cross the Fermi energy and

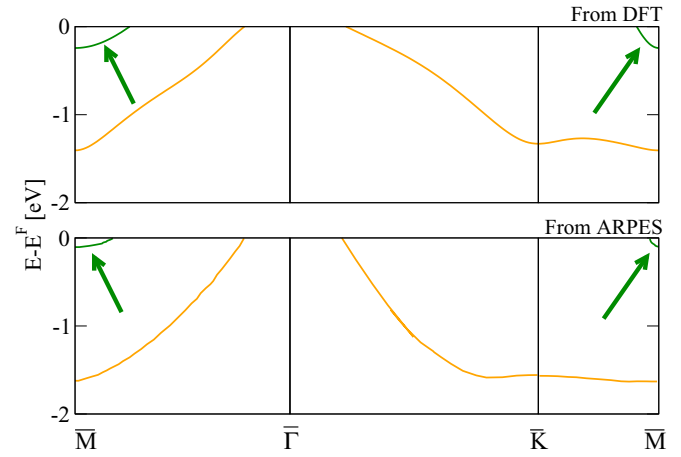


FIG. 6. Comparison of the calculated band structure (upper panel) with a schematic drawing of the extrapolated ARPES energy dispersion data (lower panel) of the DySi_2 monolayer at the Si(111) surface [20]. α and β bands are shown in yellow and green, respectively. The arrows show the position of the electron pockets.

determine the metallic character of the silicide. The first band, labeled α in Fig. 5, crosses the Fermi energy only close to the $\bar{\Gamma}$ point (acceptorlike state or hole pocket at $\bar{\Gamma}$), while the second band, labeled β , crosses the Fermi energy only close to the \bar{M} point (donorlike state or electron pocket at \bar{M}).

The first band resides completely within the bulk Si band gap, i.e., it is completely surface localized. It is almost parabolic at $\bar{\Gamma}$, however, its dispersion has a strong momentum dependence, being almost flat in $\bar{M}-\bar{K}$ direction. As discussed in Sec. IV A, an electronic state with similar energy and dispersion is also present at the nonreconstructed Si(111) surface. However, the projection of the wave function associated to the state α onto the atomic orbitals reveals that this state slightly differs from the one at the Si(111) surface. Indeed, the surface state of the pristine Si(111) is almost completely localized at the topmost Si layer. In contrast, the band α is an electronic state whose character varies through the Brillouin zone. While at $\bar{\Gamma}$ the main contribution comes from the RE- d_{z^2} and Si_3 - p_z orbital, contributions of the rare-earth s and d orbitals and Si_1 - p_z become dominant at \bar{M} .

The electronic state labeled by β in Fig. 5(a) is only occupied around \bar{M} and is a hybrid originating from the Si_2 layer and the rare-earth atoms throughout the entire Brillouin zone. Two further occupied bands with higher binding energies are predicted at \bar{K} . They are localized at the silicon/silicide interface and are due to the interaction between the rare-earth atoms and the Si substrate (Si_2 and Si_3 layer).

The calculated band structures are in agreement with available ARPES measurements [20]. The extrapolated ARPES results are compared to the calculated values (exemplarily for DySi_2) in Fig. 6. Both the position of the bands with respect to the Fermi energy as well as their dispersion are well reproduced in our calculations, which provides strong support for the validity of the structural model. Figure 7 shows a comparison between the Fermi surface predicted by DFT and the one observed in the ARPES measurements of the DySi_2 film. Again, an excellent agreement between

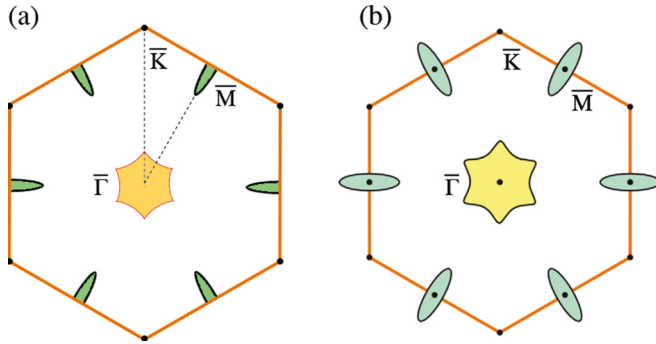


FIG. 7. Comparison of the Fermi surface of the DySi_2 monolayer calculated by DFT (a) and extrapolated from ARPES measurements (b) [20]. Elliptical states in green and hexagonlike states in yellow correspond to the electron and hole pockets described in the text, respectively.

calculated and measured data is observed. The highly eccentric ellipsoidal states centered at the \bar{M} point (in green) are related to the electron pockets shown by the arrows in Fig. 6. The pronounced eccentricity of the ellipses suggests a strongly anisotropic electronic effective mass. Indeed, an effective mass of $0.90 m_e$ is calculated along the $\bar{\Gamma}-\bar{M}$ direction, while an effective mass of $0.15 m_e$ is calculated along the $\bar{K}-\bar{M}$ direction, corresponding to a ratio of 6.1. This is very close to the values estimated by Wanke *et al.* [20] systematically analyzing ARPES energy surfaces [$(1.1 \pm 0.3) m_e$, $(0.18 \pm 0.05) m_e$, and 6 ± 2 , respectively]. The states at the Brillouin zone center (in yellow) are related to the hole pocket at the $\bar{\Gamma}$ point. The hexagonlike shape of the states is slightly concave, suggesting also in this case an anisotropic effective mass for the holelike states. The calculated values amount to $0.59 m_e$ along the $\bar{M}-\bar{\Gamma}$ direction and $0.69 m_e$ along the $\bar{\Gamma}-\bar{K}$ direction. Unfortunately, no corresponding measurements are available. However the ratio of 1.2 of the two calculated effective masses is very close to the value of 1.4 ± 0.2 estimated by ARPES [20,58].

The band structures calculated for the TbSi_2 , DySi_2 , and ErSi_2 monolayer (Fig. 5) show quantitatively very similar dispersion curves. This is not surprising, as the valence states of the investigated rare earths are identical, with minor differences in the orbital energies. This also holds for Y (the “rare earth” without f electrons). Thus the band structures calculated for Tb, Dy, and Er disilicides are comparable, and indeed very similar, to the band structures calculated by Koitzsch *et al.* [26] and by Rogero *et al.* [24] for the YSi_2 , and by Stauffer *et al.* [21] for the ErSi_2 monolayer on the Si(111) surface. This suggests that the monolayer band structures of the silicides of at least all the trivalent rare earths are qualitatively very similar.

The orbital analysis of the band structure shows that the Tb, Dy, and Er atoms in the silicide monolayers bond (covalently) to both overlying and underlying Si atoms, in a configuration that guarantees a closed-shell configuration for the rare-earth atoms and the silicon atoms of the layers Si_2 and Si_3 . A thorough discussion of the chemical bonds at the termination can be found in Refs. [21,24].

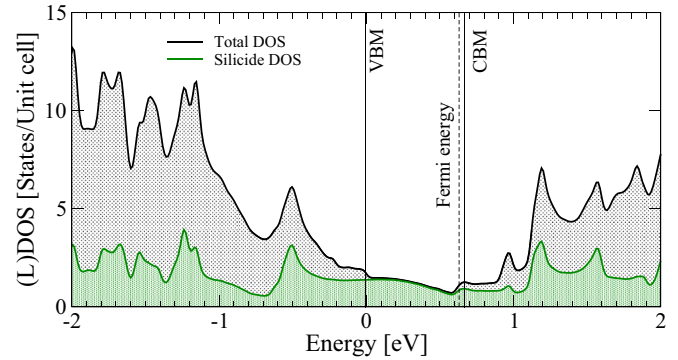


FIG. 8. Density of states calculated for the slab modeling TbSi_2 silicide at the Si(111) surface. The total DOS is shown in black, while the silicide contribution is shown in green. The zero of the energy scale labels the Si bulk valence-band maximum (VBM). The bulk conduction-band minimum (CBM) is indicated as well.

It should be also noted that the Fermi level position lies almost at the conduction-band minimum of the Si substrate with an energy deviation around 0.1 eV. This result indicates a negligible Schottky-barrier height on n -type silicon, in agreement with core-level photoemission results [7,58].

The (local) density of states—(L)DOS—in a region around the fundamental band gap is shown in Fig. 8 exemplarily for TbSi_2 . The black curve represents the total density of states of the entire slab modeling the substrate and the silicide layer. The green curve represents the local DOS of the TbSi_2 silicide layer, consisting of layers Si_1 , Si_2 , and Tb, with a boundary plane between layers Tb and Si_3 . The previously discussed surface-localized electronic states result in a nonvanishing density of states in the gap region. Here, the main contribution is due to atoms of the silicide layers. Within the plotted region, no significant differences in the (L)DOS of TbSi_2 , DySi_2 , or ErSi_2 can be observed.

Calculated and experimental STM images of the 1×1 monolayer structure are shown in Fig. 9. At positive bias electrons tunnel from the STM tip to the surface, so that empty states are mapped, while at negative bias electrons tunnel from the sample into the tip and occupied states are mapped. Considering the origin of the α and β bands as discussed above, the features observed by STM can now be assigned. For both polarities, mostly the dangling bonds of the uppermost atoms (Si_1) are imaged because of geometrical reasons. Moreover, the lower atoms of the buckled Si layer (Si_2) can also be observed because of the contribution of the β band around the \bar{M} points. Thus the complete honeycomblike structure becomes visible, and the corresponding pattern has hexagonal symmetry. The contribution of the Si_2 atoms is more pronounced at negative voltages [Figs. 9(a) and 9(c)] than at positive voltages [Figs. 9(b) and 9(d)]. No signal from the rare-earth atoms is detectable, since they are located too deep under the surface. The perfect agreement between measured and calculated STM images is a further argument for the correctness of the microscopic model for the silicide monolayer. Exactly as for the electronic band structures, also the STM images of the silicides of different rare earths are expected to be qualitatively very similar.

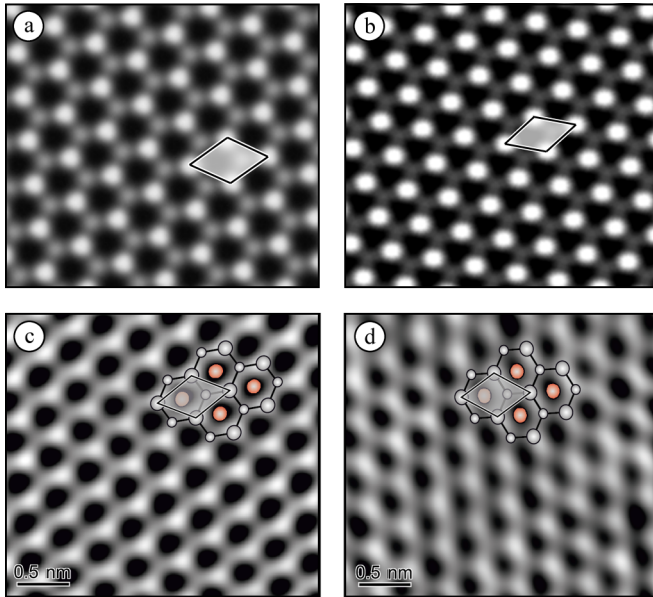


FIG. 9. Simulated filled states (a) and empty states (b) STM images of the DySi_2 monolayer with 1×1 periodicity calculated for tunneling voltages of -0.3 and $+0.3$ V, respectively. In (c) and (d), the corresponding experimental STM images of filled and empty states of the TbSi_2 monolayer are shown [12]. These were taken at tunneling voltages and currents of (c) -1.0 V and 0.5 nA and (d) $+0.3$ V and 3.5 nA. The surface unit cell is overlaid on the images.

C. The RE_3Si_5 multilayer with $\sqrt{3} \times \sqrt{3}$ superstructure

A silicide coverage exceeding one monolayer results in a $\sqrt{3} \times \sqrt{3} R30^\circ$ superstructure with RE_3Si_5 composition [1]. Planar structures consisting of exactly two silicide monolayers appear in overview STM images as domains with soft corners mainly aligned along the $[10\bar{1}]$ directions [10]. Higher structures consisting of three or more monolayers have been observed as well [10,25]. They form irregular edges without any particular orientation [10] and are often characterized by pinholes, stacking faults, and screw dislocations. While epitaxial silicide trilayers [29] and pentlayers [25] with $\sqrt{3} \times \sqrt{3}$ periodicity have been theoretically modeled in the past, we focus in this work on a coverage of two monolayers.

In the RE_3Si_5 double layer structure, the surface termination (outer silicide monolayer) has RESi_2 stoichiometry and is terminated by a buckled Si layer very similar to a Si(111) double layer (see Fig. 10) [59]. This is similar to the Si termination of the 1×1 silicide phase, as revealed by x-ray photoelectron diffraction (XPD) [59]. In contrast to the case of the 1×1 monolayer structure, this surface layer is not rotated by 180° with respect to the substrate.² The presence of an ordered array of Si vacancies in the underlying silicide layer accounts for the specific stoichiometry and explains the $\sqrt{3} \times \sqrt{3}$ periodicity observed in LEED. It has been supposed that the driving force for the formation of the vacancies is the compressive strain present in the planar silicene film parallel to the Si(111) surface, which would result in Si-Si interatomic distances about 8% shorter than in bulk Si [21].

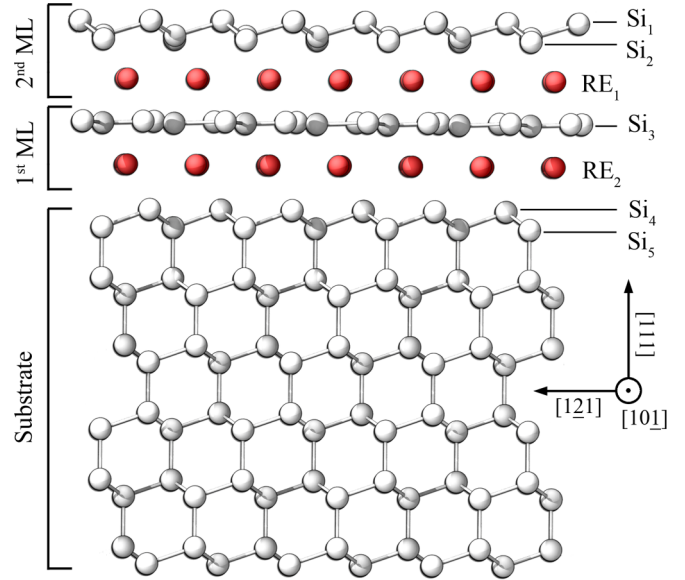


FIG. 10. Side view of the rare-earth silicide bilayer with $\sqrt{3} \times \sqrt{3}$ periodicity on Si(111). Color coding is as in Fig. 4. The topmost Si bilayer is buckled, the Si_3 layer within the silicide is silicene-like, with a vacancy superstructure. The latter is not clearly distinguishable in this side view.

Removing one Si atom from the top bilayer (Si_1 or Si_2 in Fig. 10) does not result in any strain release, as the surface layer is already buckled. Indeed, there is no experimental evidence of missing Si atoms at the top bilayer. Consequently, the Si vacancies have to be localized at the silicene-like film between the rare-earth layers (Si_3 in Fig. 10). The exact location of the Si vacancies is still argument of debate, though. Different structural models for this phase have been proposed on the basis of STM measurements by Roge *et al.* [60] and by Martín-Gago *et al.* [61,62] for Er_3Si_5 . The difference between the models lies in the position of the Si vacancies. In the first model [60], the vacancy is exactly below one of the atoms labeled by Si_1 in Fig. 10, while in the second model the vacancy lies below a Si_2 atom. In Er_3Si_5 , the silicon vacancies have been found in different studies either underneath the Si_1 [63] or Si_2 atom [61]. Engelhardt *et al.* proposed for Dy_3Si_5 a model in which the Si vacancy is located underneath the Si_2 atom, suggesting that the structure of the silicide layer with $\sqrt{3} \times \sqrt{3}$ periodicity might be different for thin and thick Er_3Si_5 and Dy_3Si_5 films [10]. Cocoltzi *et al.* found by DFT calculations for the case of Y_3Si_5 trilayers the Si_2 model energetically favored by 150 meV per $\sqrt{3} \times \sqrt{3}$ unit cell with respect to the Si_1 model [29]. Thus the position of the silicon vacancy in the thick silicide films corresponds to the energetically favored position in Si-deficient hexagonal RE_3Si_5 bulk compounds [64].

Both models discussed in the literature have been investigated in this work for Y_3Si_5 , Tb_3Si_5 , Dy_3Si_5 , and Er_3Si_5 silicide bilayers. The top view of the silicide after structural relaxation is shown in Fig. 11 for the two models. For the sake of simplicity, the rare-earth atoms at the center of the hexagons are not shown. The position of the vacancy determines different surface relaxation patterns. If the silicon vacancy is below one

²This behavior is commonly referred to as *A orientation*.

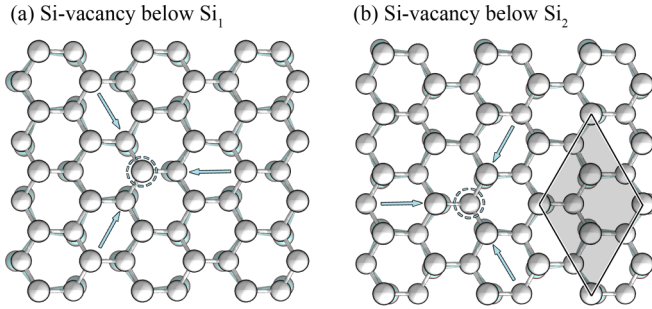


FIG. 11. Top view of the bilayer rare-earth silicide with $\sqrt{3} \times \sqrt{3}$ periodicity at the Si(111) surface. Atoms of the topmost silicon bilayer (Si_1 , Si_2) are shown in gray and atoms of the silicene-like layer (Si_3) in light blue. Rare-earth atoms in the center of the hexagons are not shown. The surface unit cell is highlighted. The arrows show the relaxation of the Si atoms in the silicene layer Si_3 toward the Si vacancies (indicated by dashed circles).

Si_2 atom [Fig. 11(b)], this atom relaxes vertically by about 0.17 Å towards the vacancy, while the neighboring atoms of the Si surface bilayer only shift slightly towards the vacancy. If the silicon vacancy is below one Si_1 atom [Fig. 11(a)], this atom experiences a smaller vertical relaxation by 0.09 Å towards the vacancy. The major structural relaxation occurs in both models in the silicene-like Si_3 layer, as the three next neighbor atoms relax towards the vacancy. The (purely lateral) relaxation directions in this plane are highlighted by the arrows in Fig. 11. The displacement magnitude is almost identical for all the investigated rare earths and amounts in both cases to 0.18 Å. The presence of the Si vacancy does not break the threefold symmetry of the surface.

Independently of the particular model, the flat rare-earth layers roughly maintain their planar structure, even if the rare-earth atoms move away from the Si vacancies. Structural details on the vertical layer positions are compiled in Table V. As in the other investigated structures, the Si-RE distances decrease with the atomic number of the involved rare earth. The distances between silicon layers underneath the silicide structure (i.e., below the Si_5 layer) deviate from the corresponding distances in bulk Si by no more than 0.01 Å. In contrast, the deviation of the RE-Si distances in the silicide films with respect to the corresponding values in the bulk silicide is rather large (up to 7%). The Si_3 layer is not exactly in between the planar rare-earth layers, but slightly closer to the RE_1 layer. Our calculations reveal that due to the presence of the Si vacancies and the consequent relaxation pattern, double monolayer RE_3Si_5 thin films have a crystallographic structure very similar to the common Si-deficient rare-earth silicides bulk phases with Th_3Pd_5 structure, while single monolayer RESi_2 silicides have the ideal (and stoichiometric) AlB_2 structure.

In our calculations, all the investigated silicide bilayers crystallize within the Si_1 model proposed by Roge *et al.* [60], i.e., with the Si vacancy located below the Si_1 atom. The Si_2 model by Martín-Gago *et al.* [61,62] is less stable by 49, 55, 54, and 53 meV per $\sqrt{3} \times \sqrt{3}$ unit cell for Y, Tb, Dy, and Er, respectively. Calculations within the LDA approximation confirm the PBE results within a few meV (e.g., 46 meV for Y_3Si_5). In both investigated models, the topmost Si bilayer is

TABLE V. Calculated distances (in Å) between atomic layers in the silicide structure with $\sqrt{3} \times \sqrt{3}$ periodicity (Si_2 model) as a function of the rare earth. See Fig. 10 for atomic labels and definitions. In brackets, the corresponding distances calculated for bulk silicides are given together with the deviation in percents.

	Y	Tb	Dy	Er
Si_1 - Si_2	0.70	0.69	0.70	0.71
Si_2 - RE_1	2.03	2.04	2.02	1.99
	(1.98)–2.5	(1.98)–2.7	(1.97)–2.3	(1.94)–2.4
RE_1 - Si_3	2.01	2.02	2.00	1.97
	(1.98)–1.5	(1.98)–1.9	(1.97)–1.6	(1.94)–1.4
Si_3 - RE_2	2.03	2.04	2.03	2.00
	(1.98)–2.5	(1.98)–2.9	(1.97)–2.7	(1.94)–3.3
RE_2 - Si_4	2.13	2.12	2.11	2.08
	(1.98)–7.6	(1.98)–7.1	(1.97)–7.1	(1.94)–7.2
Si_4 - Si_5	0.85	0.84	0.85	0.85
Si_2 - Si_3	4.04	4.06	4.02	3.95
	(3.96)–2.0	(3.97)–2.3	(3.94)–2.0	(3.88)–1.9
RE_1 - RE_2	4.04	4.06	4.03	3.97
	(3.96)–2.0	(3.97)–2.4	(3.94)–2.2	(3.88)–2.3
Si_3 - Si_4	4.16	4.17	4.14	4.08
	(3.96)–5.1	(3.97)–5.0	(3.94)–5.0	(3.88)–5.2

not rotated with respect to the substrate. A structure with the topmost bilayer rotated by 180° is, e.g., less favorable by 153 and 19 meV for the Dy_3Si_5 multilayer within the models of Roge *et al.* and Martín-Gago *et al.*, respectively, in contrast to the case of the RESi_2 monolayer.

Test calculations for Dy silicide trilayers show that silicon vacancies below the Si_1 layer are again favored (by 61 meV) with respect to vacancies located under the Si_2 layer. This is in contrast with previous theoretical investigations, where the Si_2 model by Martín-Gago *et al.* was found to be energetically favored with respect to the Si_1 model of Roge for Y_3Si_5 . Cocolletzi *et al.* estimated by DFT-PBE an energy difference of 150 meV between the two models for silicide trilayers [29]. An energy difference of 37 meV has been estimated by Rogero *et al.* within DFT-LDA for thick Y_3Si_5 pentalayers and the topmost Si bilayer rotated by 180° about the normal with respect to the Si(111) substrate [25].

The energy differences of about 50 meV calculated for the two considered models are rather small. A similar behavior is known for clean $\text{Y}_3\text{Si}_5(111)$ surfaces, where the energy difference has been estimated to 23 meV [65]. In particular, these energy differences are smaller than the thermal energy available during the silicide formation at about 500°C . Silicon vacancies below Si_1 or Si_2 atoms could thus be formed during the silicide growth, which freeze in their position during the sample cooling. As a homogeneous vacancy distribution is required to release stress from the silicene-like Si_3 layer, this could result in distinct domains with vacancies either below Si_1 or Si_2 . This may explain the observation of STM patterns compatible with both geometries in the same sample by Rogero *et al.* [25].

The electronic band structures of the silicide layers calculated with the Si_2 model are shown in Fig. 12. Due to the larger size of the surface unit cell, the Brillouin zone of the Si(111) surface is folded and the band structure

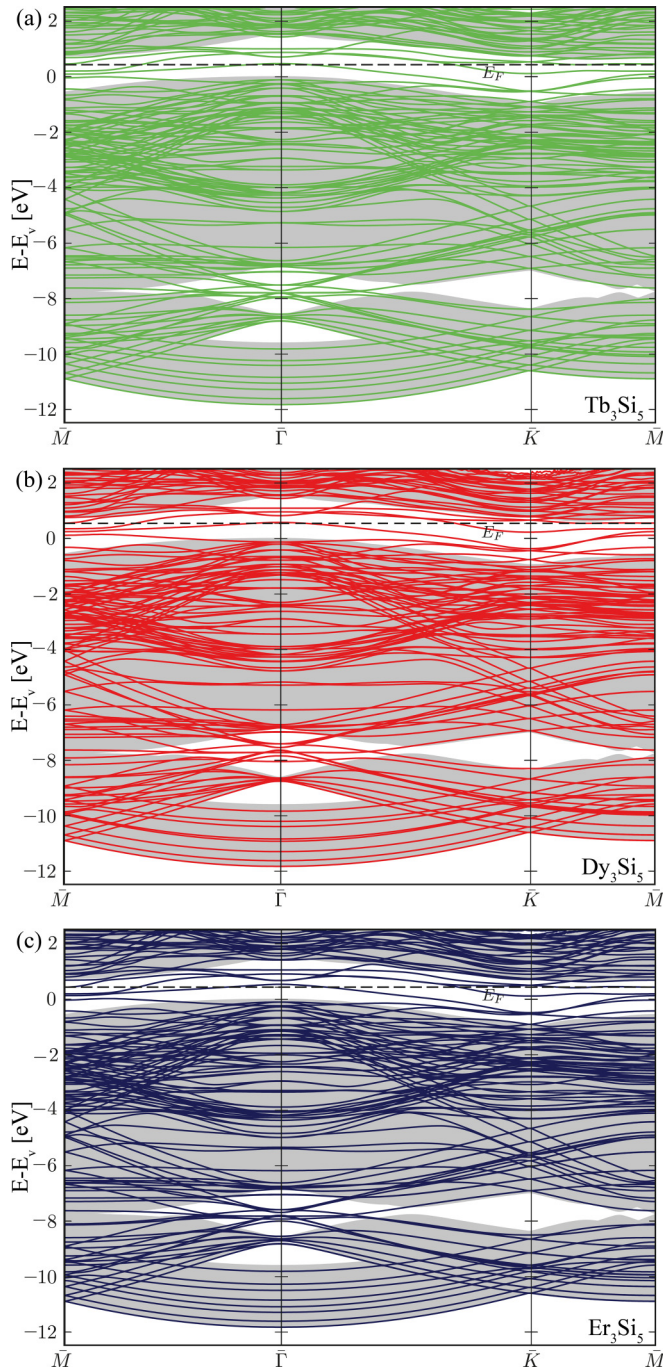


FIG. 12. Band structure of the bilayer rare-earth silicides with $\sqrt{3} \times \sqrt{3}$ periodicity on Si(111) calculated for the Si_2 model. (a) Tb_3Si_5 , (b) Dy_3Si_5 , and (c) Er_3Si_5 . Projected Si bulk bands are shaded in grey. \bar{M} and \bar{K} mark the corresponding points of the $\sqrt{3} \times \sqrt{3}$ Brillouin zone.

is correspondingly complicated. It is, however, possible to identify several states, which cross the Fermi energy and are responsible for the metallic nature of the thin films. A magnification of the gap region is shown for both Si_2 and Si_1 models in Figs. 13(a) and 13(b), respectively, in order to allow for a comparison with the bands extrapolated from ARPES measurements in Ref. [20], which are also plotted in Fig. 13(c). Two prominent states, a donorlike state (electron pocket) with

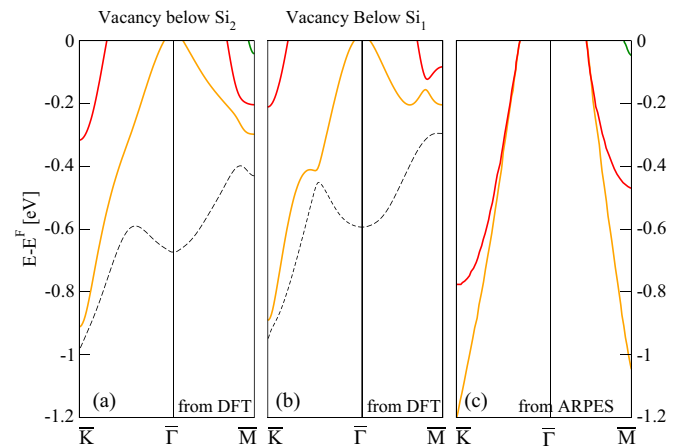


FIG. 13. Band structure of the Dy_3Si_5 bilayer on Si(111) with $\sqrt{3} \times \sqrt{3}$ periodicity. (a) Calculated according to the Si_2 model [61,62], (b) calculated according to the Si_1 model [60], and (c) schematic drawing extrapolated from the ARPES energy dispersion data [20].

a global minimum at \bar{M} (green curve), and an acceptorlike state at $\bar{\Gamma}$ (yellow curve) are identified in both DFT and ARPES measurements. The calculations closely reproduce the energetic dispersion of the donor-like state as extrapolated by ARPES. Both states can be readily identified with the corresponding bands appearing in the silicide monolayer with 1×1 periodicity. Indeed, they originate from the outmost Si bilayer and the first rare-earth layer (Si_1 , Si_2 , and RE_1). A further band (shown in red in Fig. 13) is observed by ARPES, which is qualitatively well reproduced by the theoretical models. This band has no counterpart in the monolayer silicide and is the hallmark of the $\sqrt{3} \times \sqrt{3}$ phase. From an analysis of the wave functions it is found that it stems from the defective silicene-like layer (Si_3) absent in monolayer structures. A further band (dashed black line in the lower part of the plots), which is not observed experimentally, is predicted by DFT. This band is partially covered by the substrate valence band (not shown in the picture).

The effective mass at \bar{M} in the $\bar{M}-\bar{\Gamma}$ direction of the electrons localized in the donorlike states is calculated to be $m^* = 0.13$, which indicates rather mobile charge carriers. In Ref. [20], it is suggested that the electron effective mass corresponding to these electron pockets is less anisotropic than in the silicide monolayer case, due to the different local environment of the rare earths (ideal versus Si-deficient).

The band structures of the other investigated silicides are again very similar and will not be discussed in detail. They are also comparable with the ARUPS measurements by Wetzell *et al.* [28]. Moreover, it is found that the position of the Fermi energy (about 0.4 eV below the CBM for Er_3Si_5) is much closer to the middle of the band gap with respect to the monolayer 1×1 silicides. This confirms the experimental observation that the Schottky barrier height on n -type Si rapidly increases with growing film thickness [7].

The local density of states of the slab modeling the Dy_3Si_5 silicide bilayer at the Si(111) surface (Si_2 model) in a region around the substrate fundamental band gap is shown in Fig. 14. The total DOS is represented by the black curve, while the red

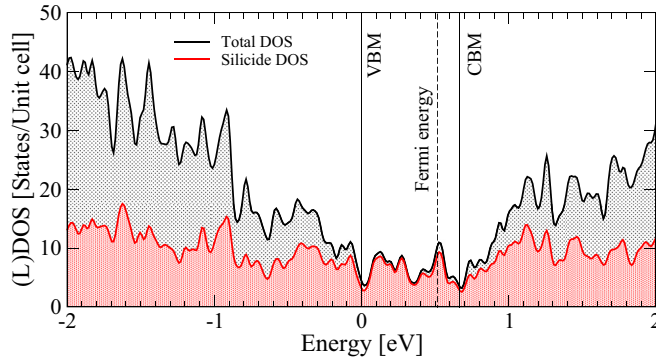


FIG. 14. Density of states calculated for the slab modeling the Dy_3Si_5 multilayer silicide at the Si(111) surface according to the Si_2 model [61,62]. The total DOS is shown in black, while the silicide contribution (layers Si_1 to RE_2) is shown in red. The zero of the energy scale labels the Si bulk valence-band maximum. The Si bulk conduction-band minimum is indicated as well.

curve represents the local DOS of the Dy_3Si_5 silicide layer. A high density of states in the substrate gap region is visible, which is almost entirely due to the silicide film. The (L)DOS of Tb_3Si_5 and Er_3Si_5 precisely match that of Dy_3Si_5 and are not shown in this work.

The calculated and measured STM images of the silicide superstructure with $\sqrt{3} \times \sqrt{3}$ periodicity are shown in Fig. 15. The images show patterns with threefold and sixfold rotational symmetry ($p3m$ for the Si_2 model and $p6$ for the Si_1 model),

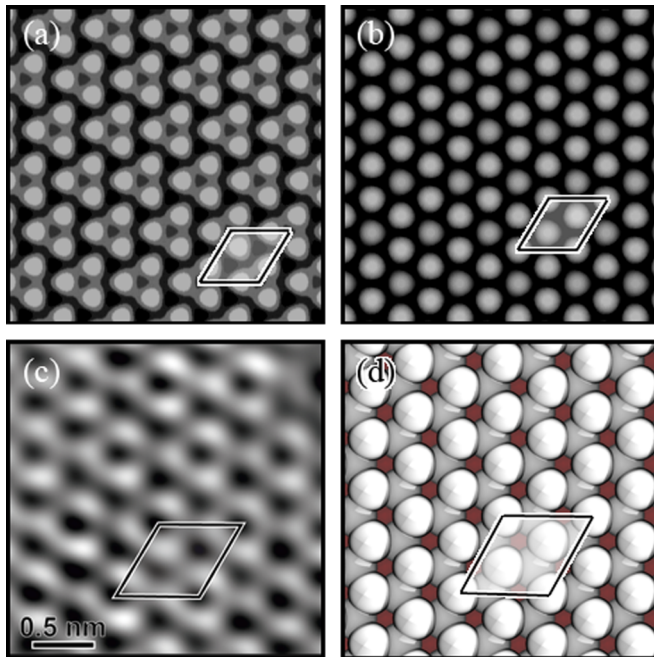


FIG. 15. Simulated (a) and (b) and measured (c) STM images of RE_3Si_5 multilayers with $\sqrt{3} \times \sqrt{3}$ periodicity on Si(111) (filled states). (a) and (b) are calculated for the Dy_3Si_5 bilayer according to the Si_2 [61] and Si_1 [60] models, respectively, at tunnel voltage of -0.3 V. Experimental images were taken for Tb_3Si_5 at -0.3 V and 4 nA. The top view of the atomic structure (identical for the two models) is shown in (d). The surface unit cell is highlighted.

which are rather different from the STM images of the silicide monolayer. This is surprising, as the surface termination of the two structures is almost identical, and suggests that the vacancies in the second silicide monolayer have a strong influence on the tunneling probability. Within the model of Roge *et al.*, a hexagonal pattern of brighter and darker spots is observed. The darker spots are assigned to the Si_1 atoms above a vacancy [Fig. 15(b)]. The images are in good agreement with the STM records by Roge *et al.* [60], which show the same pattern with $p6$ symmetry. Within the Si_2 model of Martín-Gago, brighter triangles centered at the Si_2 atom above the Si-vacancy can be discriminated [Fig. 15(a)]. As the three neighboring Si_1 atoms slightly relax toward the vacancy, darker zones appear between the triangles. The calculated pattern strictly mirrors the STM image shown for Tb_3Si_5 layers [Fig. 15(c)] as well as previously reported STM images of Martín-Gago *et al.* [62] and Engelhardt *et al.* [10] with $p3m$ symmetry. Rogero *et al.* [25] showed recently that both patterns may coexist in the same sample. This behavior agrees well with the reported observation of both patterns (Refs. [10,60,62] and Fig. 15(c)) and may be related to the rather small energy differences between the two models as compared with the thermal energies during formation at 500°C .

The constant current images simulated in our work in Tersoff-Hamann approximation clearly show the $p3m$ symmetry [Fig. 15(a)]. However, although the essential features of the experimental STM image are correctly reproduced, other details such as the darker regions between the triangles are not completely resolved in the calculated images. Simulated STM images beyond the Tersoff-Hamann model are thus necessary to correctly predict all the features of the $p3m$ pattern related to the $\sqrt{3} \times \sqrt{3}$ phase. Rogero and co-workers demonstrated that including tip effects is crucial for the STM modeling of this surface [25]. In particular, modeling the STM tip with a multiatomic tungsten structure was found to result in a better representation of the triangular grouping. Such a tip is indeed characterized by the larger extent of its s and p orbitals, yielding an enhanced current when the apex is on top of the triangle center. Nonetheless, the symmetry resulting from the STM pattern achieved with our structural model is in agreement with the experimental observation.

Thus, STM can detect the Si vacancy in the buried monolayer through the induced changes in the local density of states. The STM patterns, calculated in this work only for Dy_3Si_5 , are very similar to available measurements for both Er_3Si_5 and Y_3Si_5 . Together with the fact that the calculated band structure of Tb, Dy, and Er silicides is qualitatively similar, it is plausible that the measured/calculated STM patterns can be extended to all other multilayer silicides of trivalent rare earths with $\sqrt{3} \times \sqrt{3}$ periodicity.

D. The submonolayer $2\sqrt{3} \times 2\sqrt{3}$ superstructure

Surface x-ray diffraction studies by Lohmeier *et al.* suggested the existence of different erbium silicide phases in the low submonolayer range [8]. Although they are very important to understand dynamical processes in the silicon/silicide interface formation, submonolayer structures are far less investigated than silicide monolayers or multilayers. For rare-earth coverage up to 0.5 ML, a long ranging submonolayer

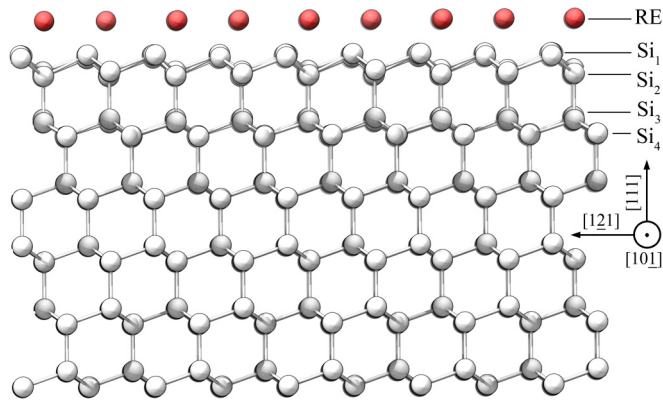


FIG. 16. Side view of the rare-earth surface layer with $2\sqrt{3} \times 2\sqrt{3}$ periodicity on Si(111). Color coding is as in Fig. 4. The rare-earth atoms form the surface termination.

reconstruction with $2\sqrt{3} \times 2\sqrt{3}$ periodicity is observed by STM [10] and LEED [see Fig. 1(b)]. The reconstruction is stable for rare-earth coverage of 0.5–1 monolayer. Thereby the STM images are interpreted as six rare earth atoms per $2\sqrt{3} \times 2\sqrt{3}$ surface unit cell arranged in a hexagonal pattern on a nonreconstructed Si(111) surface. The surface unit cell representing the deposited RE layer with RE_6 stoichiometry is composed by two nonequivalent halves. Silicides of Er [9], Dy [10], Tb [12], and Ho [66] seem to behave in a similar manner. Wetzel *et al.* pointed out that the $2\sqrt{3} \times 2\sqrt{3}$ phase is actually a metastable structure, which progressively disappears and converts into more stable silicides upon annealing [67].

In our work, we model the silicide placing the rare-earth atoms in the energetically favorable hcp positions of the pristine Si(111) surface as determined in Sec. IV A in the fashion suggested by Roge *et al.* [9] and later by Engelhardt *et al.* [10]. Indeed, it is known that when a trivalent metal is adsorbed at the Si(111) surface, all dangling bonds can be saturated if the metals are adsorbed at the threefold hcp or fcc positions [9]. In this configuration, trivalent metals typically induce $\times\sqrt{3}$ surface reconstructions [9]. Again, layers of Tb, Dy, and Er are investigated. Starting configurations with the rare-earth atoms at six different heights (from below Si_2 up to 2 Å above Si_1) have been tested (see Fig. 16 for the definitions of RE and Si_1/Si_2 layers).

After structural relaxation, the atomic positions result in the configuration shown in Fig. 17(a). This structure matches well the model extrapolated by Roge *et al.* and by Engelhardt *et al.* from STM measurements [10,67]. As shown in Fig. 16, the rare-earth atoms are not covered by a Si layer and form the surface termination. The height of the rare-earth ions above the topmost Si layer (Si_1) amounts to 1.754, 1.738, and 1.721 Å for Tb, Dy, and Er, respectively. The Si_1 and Si_2 layers relax their position with respect to the pristine Si(111) surface in order to accommodate the rare-earth atoms. These sit only roughly at the initial hcp position and form distorted hexagonal rings with three short ($d_S = 3.60$ Å) and three long edges ($d_L = 4.09$ Å). These are marked in Fig. 17(a) by S (short) and L (long), respectively. Due to this pronounced distortion with respect to the ideal hcp positions ($\Delta d = 13.5\%$), the structure has threefold rather than sixfold rotational symmetry.

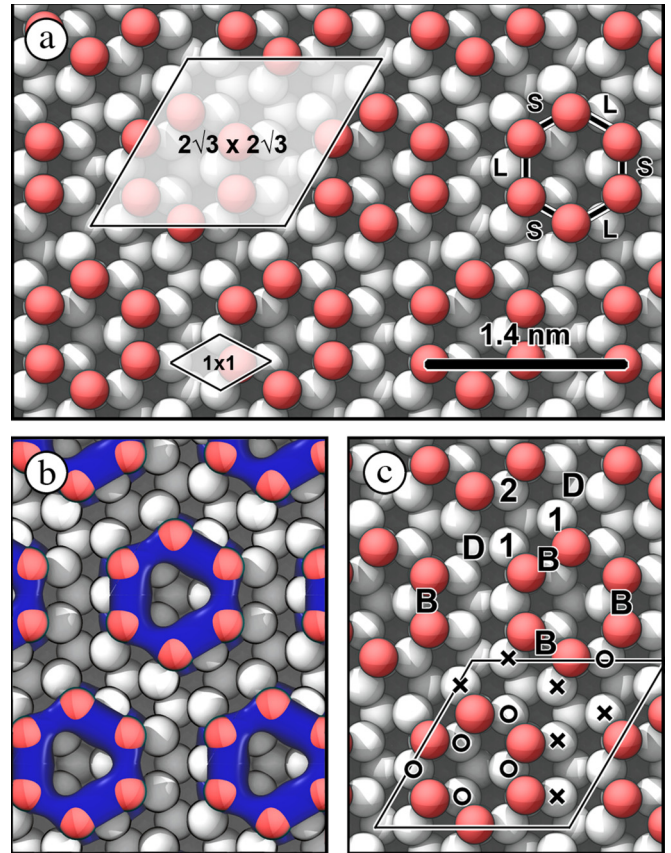


FIG. 17. (a) Top view of the rare-earth surface layer with $2\sqrt{3} \times 2\sqrt{3}$ periodicity on Si(111). Color coding is as in Fig. 4. The surface unit cell is highlighted, the smaller 1×1 surface unit cell is shown for comparison. (b) Isosurface of $0.0035 \text{ eV}/\text{Å}^3$ for the squared wave function corresponding to the uppermost occupied state. (c) Top view of the surface as in (a). The meaning of the labels is described in the text.

In the resulting configuration, each of the twelve Si dangling bonds of the surface unit cell (one for each of the 12 topmost Si atoms) is saturated by one electron from the six rare-earth atoms. The remaining electron of the trivalent rare earths is supposed to form a delocalized hybrid orbital at the rare-earth ring, similar to the delocalized orbitals of benzene. Such an electronic configuration is assumed to stabilize the rare-earth rings [67]. In order to verify this assumption, we have calculated the squared wave functions corresponding to the band edges. An isosurface of the squared wave function associated to the valence band maximum integrated over the whole Brillouin zone is shown in Fig. 17(b). As expected, the calculations predict a delocalized hybrid orbital at the RE_6 ring, reminiscent of the delocalized benzene orbital. Both the highest occupied valence-band and the lowest unoccupied conduction-band states have similar shape. The distorted form of the Dy pattern suggests the presence of two nonequivalent rare-earth positions within the ring. This is interpretable as a Peierls-like distortion that further enhances the ring stability by increasing the splitting between bonding and antibonding states formed by the rare-earth orbitals in the ring [67].

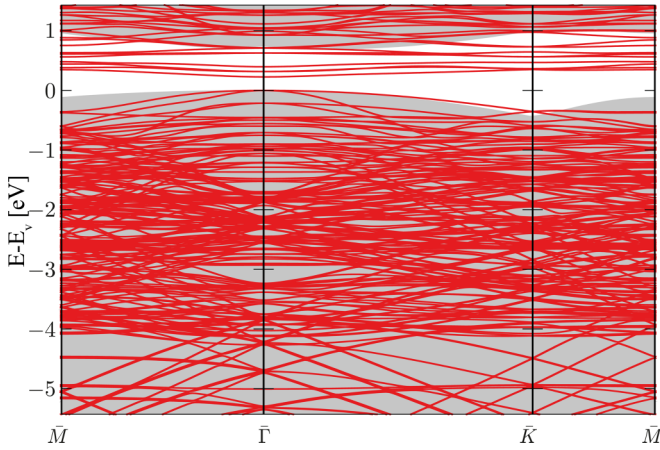


FIG. 18. Calculated band structure of the submonolayer Dy silicide with $2\sqrt{3} \times 2\sqrt{3}$ periodicity at the Si(111) surface. \bar{M} and \bar{K} mark the corresponding points of the $2\sqrt{3} \times 2\sqrt{3}$ Brillouin zone. Projected bulk bands are shown in grey.

The calculated electronic structure of the silicide is shown in Fig. 18. Thereby \bar{M} and \bar{K} mark the corresponding points of the $2\sqrt{3} \times 2\sqrt{3}$ Brillouin zone. The calculated band structure is characterized by a high density of states with a minor dispersion and with very similar energies, which are also present within the Si bulk band gap. This is due to the multiple folding of the 1×1 Brillouin zone in the larger $2\sqrt{3} \times 2\sqrt{3}$ surface unit cell. Despite the presence of several states within the fundamental gap, none of them crosses the Fermi energy, and a small energy gap of about 0.23 eV at the $\bar{\Gamma}$ point is preserved, as also expected from the Peierls-like distortion. The band gap is also evident from the plots of the DOS shown in Fig. 19.

The simulated and measured STM images of the submonolayer silicide with $2\sqrt{3} \times 2\sqrt{3}$ periodicity at the Si(111) surface termination are shown in Fig. 20. We remark that the experimental STM images with Tb [Figs. 20(c) and 20(d)] are very similar to those with Dy [10]. They show a high density of domain boundaries (indicated by the straight lines) separating

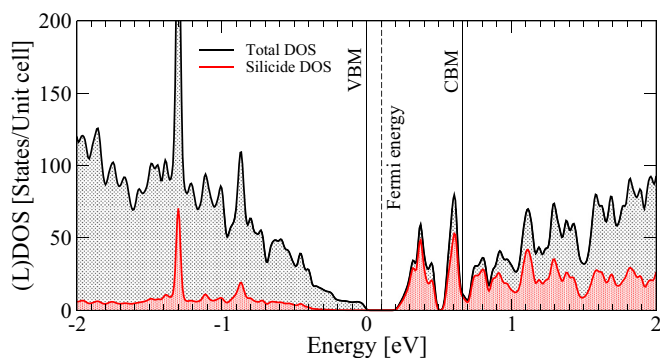


FIG. 19. Density of states calculated for the slab modeling the $2\sqrt{3} \times 2\sqrt{3}$ reconstructed Dy_6 submonolayer structure at the Si(111) surface. The total DOS is shown in black, while the contribution from the Dy_6 rings is shown in red. The zero of the energy scale labels the Si bulk valence-band maximum. The Si conduction-band minimum is indicated as well.

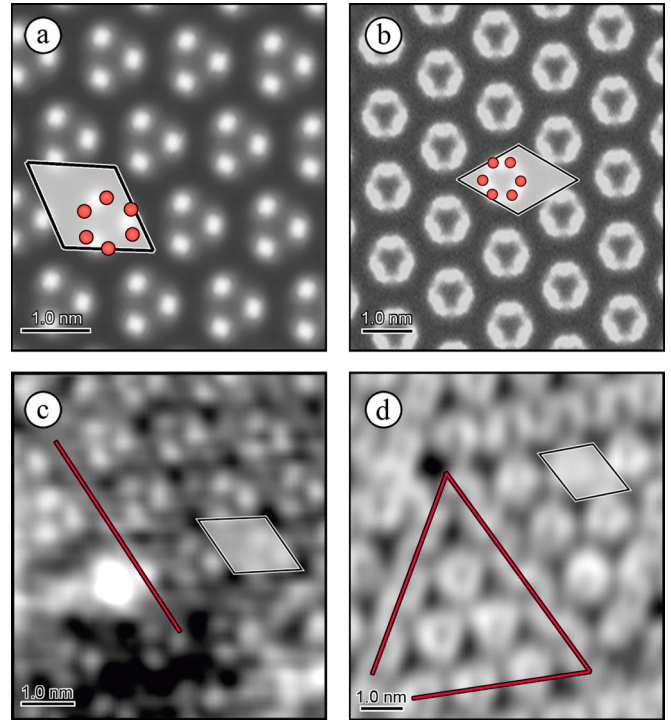


FIG. 20. Simulated [(a) and (b)] and measured [(c) and (d)] STM images of the $2\sqrt{3} \times 2\sqrt{3}$ reconstructed rare-earth silicide submonolayer at the Si(111) surface. Simulated STM images are calculated for the Dy_6 structure at tunneling bias of (a) -0.3 V and (b) $+0.3$ V, while measured images were taken for the Tb_6 structure at tunneling biases and tunneling currents (c) -2.5 V and 100 pA and (d) $+1.5$ V and 100 pA. (a) and (c) are filled state and (b) and (d) empty state STM images. Straight lines show the position of domain boundaries. The surface unit cell is indicated.

domains with $2\sqrt{3} \times 2\sqrt{3}$ periodicity. They are related to stress compensation effects [12], which are not accounted for in our theoretical models.

In order to interpret the STM images, a thorough understanding of the surface chemical bonds is necessary. The twelve Si atoms at the topmost surface layer can be divided in two groups. Six of them, labeled by circles in Fig. 17(c), are each bound with two rare-earth atoms and the other six, labeled by crosses in Fig. 17(c), with only one. Two of the Si atoms between the neighboring rare-earth hexagons are bound with two rare-earth atoms and one with a single rare-earth atom. They are marked by **2** and **1** in Fig. 17(c), respectively. This gives rise to different darker and brighter regions in the measured filled states STM images shown Fig. 20(c). A comparison with the simulated filled states STM [Fig. 20(a)] reveals that the brighter triangular features correspond to the charge accumulation at the shorter bonds of the rare-earth hexagons. The position of the brighter spots is marked by **B** in Fig. 17(c). While the overall appearance of the simulated STM images matches well the experimental results, the darker regions at the surface unit cell corners are not markedly enough reproduced. Darker regions in the filled states STM image correspond to three neighboring Si atoms bound with a single Dy atom [marked by **D** in Fig. 17(c)]. The reduced accuracy of the simulated STM is probably due to the limitations of the

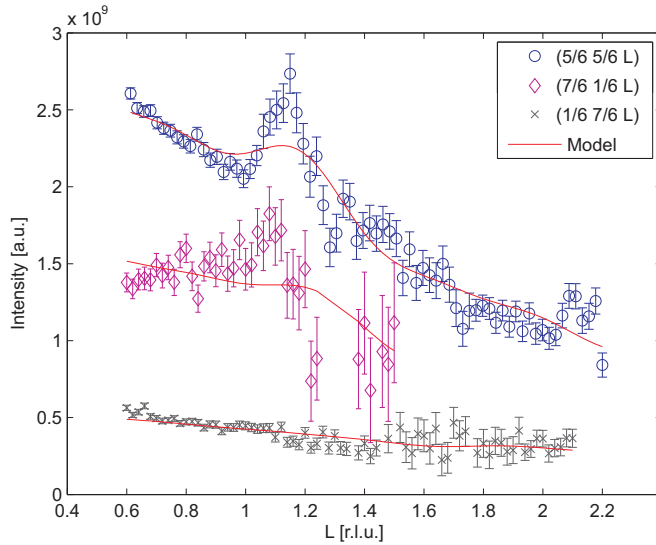


FIG. 21. Comparison of the experimentally obtained SXR intensity of various Dy silicide $2\sqrt{3} \times 2\sqrt{3}$ superstructure rods (blue crosses) with data calculated from the structural model obtained in this work (red lines).

Tersoff-Hamann approximation. More refined approaches for the simulation of STM images based on the explicit calculation of electronic transport are required to clarify this point. A thorough discussion of the filled states STM images can be found in Ref. [10].

Concerning the empty states [Figs. 20(b) and 20(d)], a pattern consisting of regular figures with hexagonal shapes is observed in the measured and in the simulated STM images. Due to the lower electronegativity of the rare earths with respect to Si, mainly the lanthanide atoms are imaged in empty states STM images. Indeed, the calculated and measured pattern is similar to the delocalized π antibonding orbital formed at the rare-earth rings.

In addition, *in situ* SXR experiments were performed on the $2\sqrt{3} \times 2\sqrt{3}$ structure to obtain complementary data. Here, we focus on the most intense superstructure Bragg rods, which are exclusively caused by this structure. We do not consider other rods, which can be influenced by the coexistence with $\sqrt{3} \times \sqrt{3}$, 2×5 or 2×1 silicide phases, as shown in Ref. [12].

Figure 21 compares background corrected diffraction intensities obtained for superstructure Bragg rods ($H; K$) (blue crosses) and intensities calculated from the structural model of the $2\sqrt{3} \times 2\sqrt{3}$ structure developed in this work (red lines). Here, ($H; K$) denote the indices of the Bragg rods using the hexagonal basis of the Si(111) surface. The third index L is related to the vertical component Q_{\perp} of the scattering vector via $L = Q_{\perp}d/2\pi$ presented in reciprocal lattice units (r.l.u.) where d denotes the distance between Si(111) crystal planes.

The L scans show quite smooth variations of the diffraction intensity. This effect can mainly be attributed to the planar structure of the Dy layer since the diffracted intensity is mostly influenced by waves scattered at Dy atoms due to their much higher atomic form factor compared to Si. Therefore perpendicular to the surface, no interference effect between scattered partial waves from Dy atoms is expected due to the flat Dy layer. Nevertheless, the (5/6;5/6) superstructure

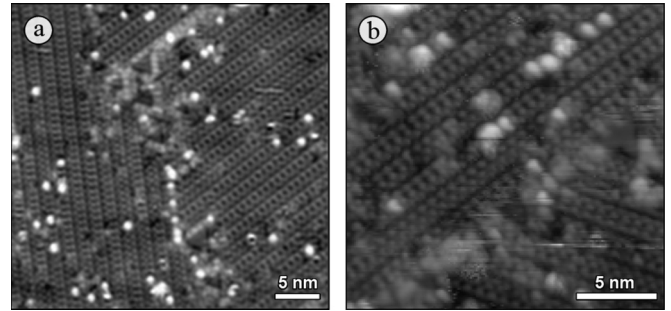


FIG. 22. Measured filled states STM images of the 5×2 terbium silicide submonolayer at the Si(111) surface achieved for sample voltages of -2.0 V and tunneling currents of 100 pA [12].

rod clearly shows a prominent peak at $L = 1.15$, which can also be guessed for the (7/6;1/6) superstructure rod. Therefore this intensity has prominently to be related to the interference between the scattered partial waves from Dy atoms interfering with scattered waves from Si atoms.

Superstructure rods, however, are only influenced from atoms with positions deviating from the 1×1 bulk structure. Therefore one only has to consider the very first reconstructed Si bilayers. On first sight, the enhanced intensity can be attributed to the constructive interference between the Dy layer and the bottom Si layers (Si₂ and Si₄ in Fig. 16), while the top Si layers (Si₁ and Si₃) interfere almost destructively for this diffraction condition. We expect that these top Si layers would reveal constructive interference for $L > 2$. However, for this diffraction condition, the intensity is very small due to the Debye Waller factor. Compared to these simple considerations, we also like to emphasize that the analysis is further complicated due to the parallel component of the scattering vector that gives some further interference effects, which are beyond the discussion presented here.

E. The submonolayer 5×2 superstructure

A further silicide film with 5×2 periodicity is formed at the Si(111) surface for submonolayer rare-earth coverage. 5×2 silicide phases of Gd [11,68], Tb [12], Dy [10], Ho [66], and Er [67] have been observed. This structure consists of a silicide submonolayer termination and is—exactly as the $2\sqrt{3} \times 2\sqrt{3}$ phase—metastable [67]. The two structures are in competition for low rare-earth coverage, however, both are transformed into more stable silicides upon annealing. The STM image of terbium silicide shown in Fig. 22(a) reveals chainlike structures in the $[1\bar{1}0]$ direction (three equivalent chain orientations are thus possible). In more detailed images [Fig. 22(b)], two to four protrusions are observed per 5×2 unit cell, depending on the tunneling conditions.

However, without precise knowledge of the rare-earth content, it is hard to extract structural information from the STM images. Consequently, very few attempts to assign a structural model to the rare-earth film are available in the literature [11,12]. We remark that the 5×2 reconstruction observed in this work occurs clearly in the submonolayer regime and is thus different from the reports in Ref. [25], in which silicide films of 5–10 monolayers are discussed.

Correspondingly, the models proposed in Ref. [25], partially involving buried silicides, do not describe the films observed in this work.

In order to develop a model for the 5×2 superstructure, several factors can be considered. First of all, the stable silicides depend on the lanthanide coverage. In detail, for growing rare-earth availability the occurring structures are the $2\sqrt{3} \times 2\sqrt{3}$ reconstruction, followed by the 5×2 and then by the 1×1 . Considering the size of the respective surface unit cells, this limits the number of rare-earth atoms to a maximum of ten atoms per surface unit. Furthermore, the STM images of Fig. 22 reveal the presence of ordered chains along the $[1\bar{1}0]$ direction. Thus the rare-earth atoms are placed in our models in the stable positions determined in Sec. IV A, so that oriented chain-like structures are formed. As the rare-earth atoms in silicide films with 1×1 periodicity are completely covered by a silicon double layer that is absent in the films with $2\sqrt{3} \times 2\sqrt{3}$ periodicity, it is plausible that the lanthanide ions in the 5×2 phase are at least partially covered by Si atoms. Therefore rare-earth layers covered to a different extent are simulated. In order to capture possible Si dimerization effects as known from other silicon surfaces—e.g., the Si(001)—doubled 5×1 unit cells with artificial dimerization in the $[1\bar{1}0]$ directions are employed. Models consisting of alternating Si Seiwatz and honeycomb chains with rare-earth atoms in between, as originally proposed by Battaglia *et al.* [11] and then by Franz *et al.* [12], have been tested as well.

Following the criteria above, we have developed 14 structural models, which are shown in Figs. 23 and 25. Besides the model name [a to n, corresponding to Figs. 23(a)–23(n)], the number of rare-earth atoms per 5×2 unit cell is indicated in the picture. Further models are conceivable, however, our model pool should cover a sufficiently high number of combinations of the explained criteria to draw general conclusions. As the slabs modeling the surface structures contain a different number of Si and rare-earth atoms, their DFT total energy cannot be directly compared. In order to determine the thermodynamically stable structures, we calculate the Landau potential as described in Sec. II B. As neither the contribution to the free energy of the hydrogen atoms nor the size of the surface unit cell are considered for this particular calculation, the calculated values do not correspond to the absolute formation energies of the structures and the Landau potential is labeled by Ω' . However, as both the surface unit cell as well as the number of hydrogen atoms used to passivate the dangling bonds at the bottom side of the slabs are the same for all configurations, a relative comparison of the different structures is possible. Even if the 5×2 phase has been observed for different rare earth silicides, we limit our investigation to Dy silicide due to the high demand of computational resources. However, based on our experience with the other silicide structures discussed above, the results may again be extrapolated to all trivalent rare earths.

The results of the calculations are shown in Fig. 24. It should be noted first that the structures labeled by c, e and g, employed to model surface dimerization effects, relaxed back to a structure with 5×1 periodicity and cannot therefore model the observed 5×2 silicides.

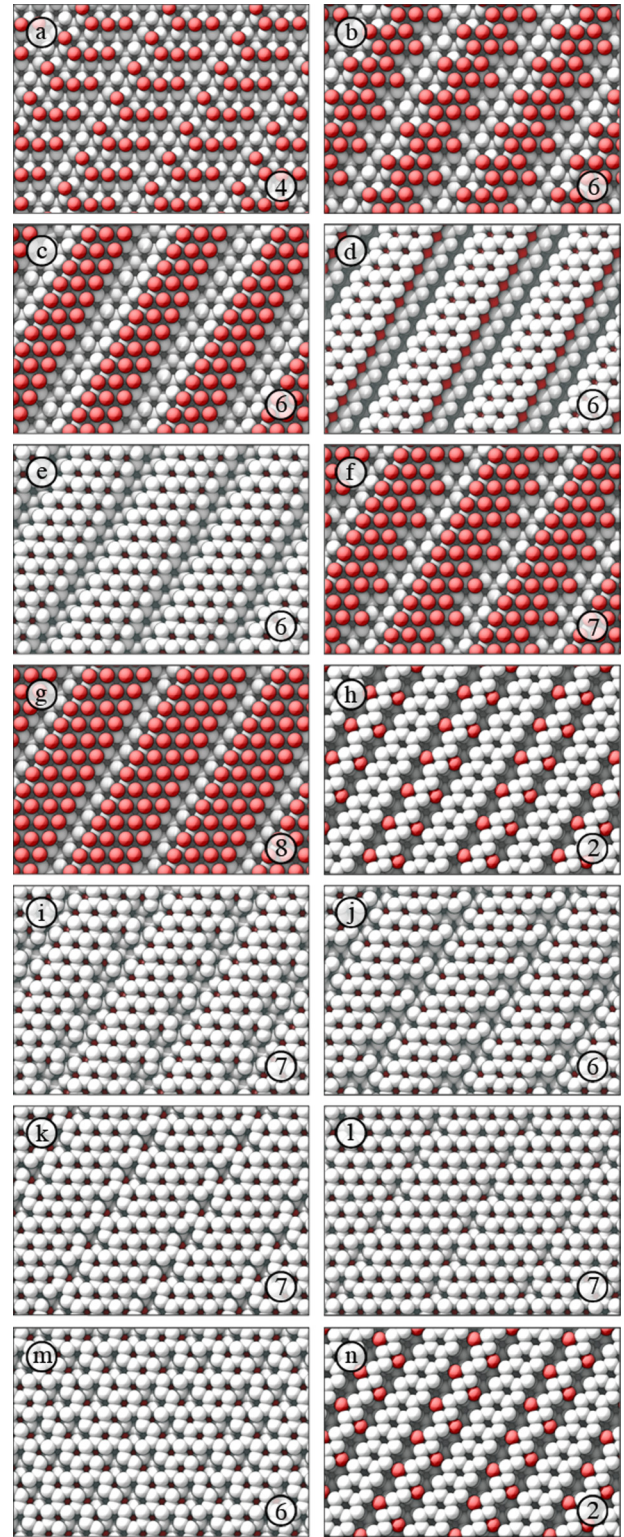


FIG. 23. Top view of the relaxed structures modeling the rare-earth induced surface reconstruction with 5×2 periodicity on the Si(111) surface. The numbers in the lower right corner indicate the number of rare-earth atoms per surface unit cell. Color coding is as in Fig. 4.

A first glance at the phase diagram reveals that structures with rare-earth atoms in the channels between honeycomb and Seiwatz chains (h,n) are favored. Indeed, for most values of

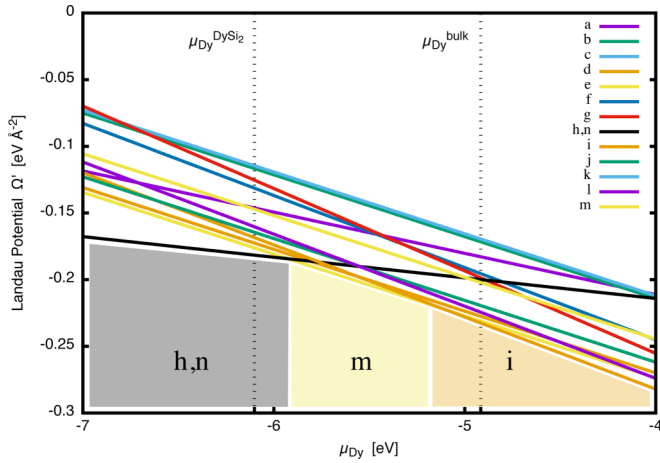


FIG. 24. Calculated phase diagram for the dysprosium adsorbed Si(111) surface with 5×2 periodicity as a function of the dysprosium chemical potential μ^{Dy} . Two representative values of μ^{Dy} , corresponding to Dy in its metallic hcp bulk phase and to Dy in hexagonal DySi₂ state are indicated. Si-rich conditions are assumed.

the chemical potentials, which are relevant for submonolayer coverage, the structures labeled by *h* and *n* are the most stable configurations, while for strongly Dy rich conditions the models *m* and *i* can be formed. These structures are less relevant, however, since at these values of the rare-earth chemical potential monolayer or multilayer silicides are formed, as we will show in the following.

Thus, the energetically almost degenerate models *h* and *n* (energy difference 18 meV per 5×2 unit cell) with two rare-earth atoms per unit cell describe the observed phase. Considering that four and eight Si atoms per 5×2 unit cell build the Seiwatz and honeycomb chains, respectively, the stoichiometry of the silicide layer at the Si(111) surface can be expressed as RESi₆. The difference between the two models *h* and *n* consists in the different alignments of neighboring rare-earth atom rows on both sides of the honeycomb chains. The slightly more stable model *h*, in which the rare-earth atoms are aligned in-phase, is shown in more detail in Fig. 25. It is known that on Si(111) a honeycomb chain is stabilized by one electron per 3×1 unit cell, while a zig-zag Seiwatz

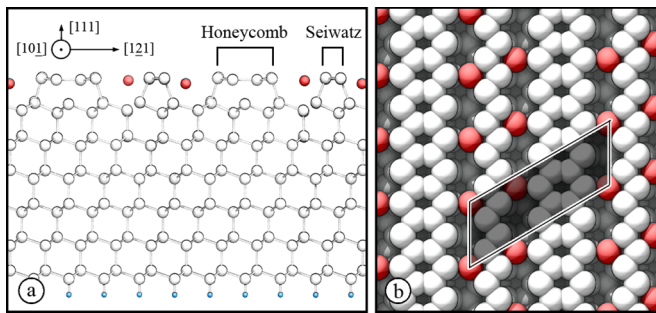


FIG. 25. Side (a) and top view (b) of the thermodynamically stable rare-earth induced surface reconstruction with 5×2 periodicity on the Si(111) surface. The termination corresponds to structure *h* in Figs. 23 and 24 and consists of alternating Si Seiwatz and honeycomb chains. Color coding is as in Fig. 4. The surface unit cell is highlighted.

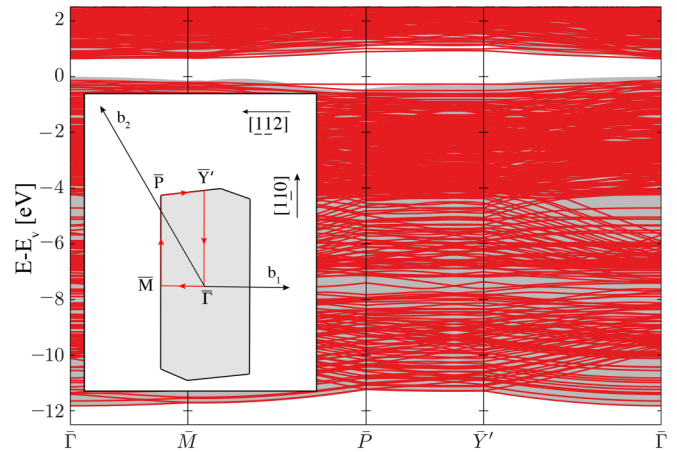


FIG. 26. Electronic band structure calculated for the slab modeling the Si₆ silicide with 5×2 periodicity on the Si(111) surface according to the model labeled by *h* in Figs. 23 and 24. The zero of the energy scale labels the valence-band maximum. Projected bulk bands are shown in grey. The inset shows the surface Brillouin zone of the 5×2 structure.

chain requires two electrons per 2×1 unit cell [11]. Thus the 5×2 phase can be thought of as being built of two 3×1 surface units with honeycomb chains and two 2×1 surface units containing Seiwatz chains. The structure is stabilized by two trivalent rare-earth atoms, which provide six electrons per unit cell.

Figure 26 shows the calculated electronic band structure of model *h*, which strongly resembles the projected Si-bulk electronic structure. Almost no surface localized electronic states are present in the gap region. The fundamental electronic gap (direct, at $\bar{\Gamma}$) is only slightly smaller than the calculated Si bulk gap. This confirms that the submonolayer silicide with 5×2 periodicity on the Si(111) surface is semiconducting. The inset of Fig. 26 shows the high-symmetry points of the 5×2 surface Brillouin zone employed for the calculations. Due to the overall low symmetry typical for oblique surface cells, the reciprocal vectors do not cross the corner points of the first Brillouin zone. The atomic chains are parallel to the Γ - Y' direction.

The (local) density of states of the slab modeling the DySi₆ silicide with 5×2 periodicity on the Si(111) surface is shown in Fig. 27. The total density of states is represented by the black curve, while the red curve represents the local DOS of the silicide layer. The dotted lines indicate the valence and conduction-band edges of bulk Si. The calculated (L)DOS again shows that the silicide layer is semiconducting. The overall appearance of the total DOS is very similar to the Si bulk DOS, with the exception of a minor reduction of the fundamental band gap. This effect is due to the electronic states close to the conduction-band minimum. Otherwise, the presence of the DySi₆ layer does not strongly affect the band-gap region of the substrate.

The knowledge of the thermodynamically stable structural model now also allows for the interpretation of the STM images and the identification of the observed features. In the filled state images [Figs. 28(a) and 28(c)], the bright spots are assigned to the honeycomb (broad rows) and Seiwatz (thin

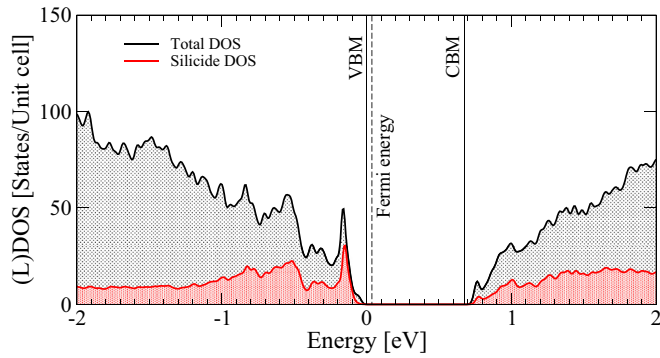


FIG. 27. Density of states calculated for the slab modeling the DySi_6 silicide with 5×2 periodicity on the Si(111) surface according to the model labeled by h in Figs. 23 and 24. The total density of states is shown in black, while the silicide contribution is shown in red. The zero of the energy scale labels the Si bulk valence-band maximum. The Si bulk conduction-band minimum is indicated as well.

rows) chains, which capture the electrons from the rare-earth atoms. The latter are thus not visible at this bias. In contrast, in the empty state images [Figs. 28(b) and 28(d)], the rare-earth atoms donating their electrons are visible, while the dark rows show the location of the honeycomb chains. As between the chains different equivalent lattice sites are available for the rare-earth atoms, different STM patterns are possible. These correspond to an in-phase alignment between neighboring rare-earth rows (model h) or a zigzag alignment (model n).

In contrast to monovalent and divalent ions, for which also other $n \times 2$ phases with odd $n \neq 5$ have been observed, 5×2 is the only possible $n \times 2$ periodicity for trivalent rare earths.³ Sticking to the models consisting of alternating honeycomb and Seiwatz chains, phases of 7×2 or 9×2 periodicity could, in principle, be built by one honeycomb chain and two or three Seiwatz chains, respectively. These structures, however, would have to be stabilized by 10 and 14 electrons per unit cell, respectively. This condition cannot be satisfied by an integer number of trivalent donors, which explains why no other $n \times 2$ phase than the 5×2 has been observed for trivalent rare earths.

F. Surface stability

In order to compare the relative stability of the investigated silicide films and to understand at which thermodynamic conditions they are formed, we calculated their formation energy as a function of the rare-earth chemical potential, as described in Sec. II B. The complete phase diagram shown in Fig. 29 is exemplarily computed for dysprosium silicide,

³It is also important to notice that the adsorption of divalent metals at the Si(111) typically leads to a $n \times 2$ surface reconstruction, with n an odd integer. Thus, as suggested by Battaglia *et al.* [11], 5×2 phase might be induced by divalent lanthanides such as Yb, Eu, Sm, or Tm. In this case, they would give rise to completely different structures, similar to the reconstructions formed by deposition of divalent alkaline-metal earths (Mg, Ca, Sr, and Ba). These are not investigated in this work, as we only consider lanthanides in the trivalent state (Dy^{3+} , Tb^{3+}).

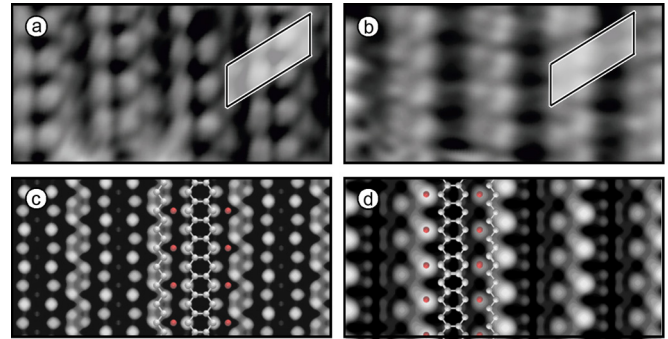


FIG. 28. (a) and (b) Measured STM images of the 5×2 Tb silicide submonolayer structure on the Si(111) surface [12] and (c) and (d) corresponding simulated STM data for Tb. Experimental STM images are taken for sample voltages of -1.5 V [(a) and (c) filled states] and $+1.5$ V [(b) and (d) empty states], and tunneling currents of 100 pA. The 5×2 surface unit cell is indicated.

as the 5×2 phase has only been modeled for dysprosium silicide. The Dy chemical potential μ_{Dy} represents the growth conditions. On the left-hand side of the chemical potential axis, there are Dy-poor conditions, while regions at the right-hand side represent Dy-rich conditions. Two particular values are highlighted by dotted lines in the phase diagram, labeling the values of μ_{Dy} for bulk metallic dysprosium and for Dy in stoichiometric DySi_2 bulk silicide under Si-rich conditions. For chemical values smaller than $\mu_{\text{Dy}}^{\text{DySi}_2}$, nonstoichiometric DySi_x silicides can be formed at the surface, while for $\mu_{\text{Dy}} > \mu_{\text{Dy}}^{\text{Bulk}}$ metallic dysprosium segregation at the Si(111) surface occurs. Between the two values the Dy availability changes continuously. Since surfaces can equilibrate much faster

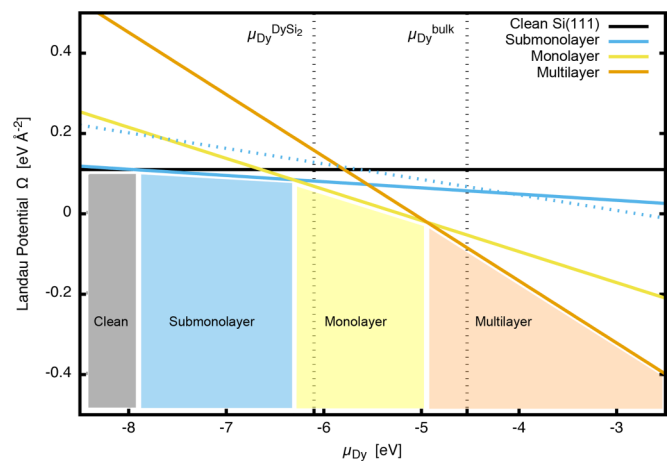


FIG. 29. Calculated phase diagram of the dysprosium adsorbed Si(111) surface as a function of the rare-earth availability. The latter is represented by the dysprosium chemical potential μ^{Dy} . Two representative values of μ^{Dy} , corresponding to Dy in its metallic hcp bulk phase and to Dy in the hexagonal DySi_2 state are indicated. Si-rich conditions are assumed. The curve for the submonolayer silicide represents the phase with 5×2 periodicity, while the dotted line shows the formation energy of the metastable structure with $2\sqrt{3} \times 2\sqrt{3}$ periodicity. “Clean” labels the unreconstructed, Dy-free Si(111) surface.

than the bulk phases, also values of the chemical potentials beyond the indicated references are considered in the phase diagram.

The main outcome of the phase diagram is that, depending on the growth conditions, a variety of silicide phases with different Dy content may occur. For Dy-poor conditions, clean Si(111) surfaces are formed. For growing values of μ_{Dy} , submonolayer phases with 5×2 periodicity, and then monolayer structures with 1×1 periodicity are formed. For Dy-rich conditions, multilayer structures with $\sqrt{3} \times \sqrt{3}$ periodicity are thermodynamically favored. It is observed in the phase diagram that the submonolayer structure with $2\sqrt{3} \times 2\sqrt{3}$ periodicity is metastable (dotted line in Fig. 29). It does not represent a thermodynamically stable equilibrium state, but is formed due to kinetically limited growth. This is also underlined by the adsorption-like structure with RE_6 rings on an unreconstructed Si(111) surface, while the more stable 5×2 phase is characterized by rare-earth atoms embedded within Si chains, resulting in a more stable structure (similar as the monolayer and multilayer silicides).

For very low values of μ^{Dy} (left-hand side), when not sufficient dysprosium is available to form ordered submonolayer structures, the rare-earth atoms are adsorbed at the Si(111) 7×7 surface in form of isolated ions. A rare-earth coverage lower than 0.1 ML does not alter the 7×7 periodicity and results in the formation of different types of ordered clusters of rare-earth atoms in one half Si(111) 7×7 unit cell [69]. Two cluster types, differing in their orientation within the 7×7 half unit cells, are possible [12]. Similar clusters, sometimes referred to as *magic clusters*, are also formed on Si(111) 7×7 by other metals [70–73]. For the sake of simplicity, they are not represented in the phase diagram.

V. CONCLUSIONS

Two-dimensional silicide structures of different periodicity formed at the Si(111) surface upon rare-earth deposition have been prepared and investigated by a combination of theoretical and experimental techniques. Thereby information concerning the surface periodicity could be extracted by diffraction measurements (LEED), whereas information about the silicide surface structure at the atomic scale could be obtained by STM and XRD measurements. The dispersion of the electronic states was measured by ARPES. DFT models allowed for the identification and assignment of a structural model compatible with the experimental results for the different silicide structures.

The deposition of one monolayer of rare-earth silicide results in a metallic, almost defect free RESi_2 thin film. The uppermost Si layer can be thought of as a distorted honeycomb plane (silicene-like), in which one of the two Si atoms of the unit cell is displaced outwards. The resulting buckled surface is similar to the unreconstructed bulk Si(111) surface. The corresponding band structure shows metallic surface states related to both Si and rare-earth atoms, and allows for the interpretation of the chemical bond between the atoms. The Fermi level position lies almost at the conduction-band minimum of the Si substrate, which indicates a negligible Schottky-barrier height on n -type Si.

At higher rare-earth coverage, metallic multilayer structures such as silicides with $\sqrt{3} \times \sqrt{3}$ periodicity can be observed. DFT models predict a silicide layer with RE_3Si_5 stoichiometry. The presence of Si vacancies in a planar, silicene-like film between two rare-earth planes accounts for the Si deficient stoichiometry. The Fermi energy position close to midgap for the multilayer structures confirms the experimental observation that the Schottky-barrier height rapidly increases with the film thickness.

At lower rare-earth coverage, submonolayer structures such as a termination with $2\sqrt{3} \times 2\sqrt{3}$ periodicity and RE_6 stoichiometry, as well as a phase 5×2 periodicity are formed, instead. While the phase with $2\sqrt{3} \times 2\sqrt{3}$ periodicity consists of slightly distorted rare-earth hexagons forming regular patterns on the unreconstructed Si(111) surface, the 5×2 structure is characterized by alternating Si honeycomb and Seiwatz chains oriented along the $[10\bar{1}]$ crystallographic direction. The rare-earth atoms are located in the channels between the chains. While the formation of the silicide structures with 5×2 periodicity does not strongly affect the electronic properties of the substrate, the presence of the silicide layer with $2\sqrt{3} \times 2\sqrt{3}$ periodicity strongly reduces the fundamental band gap to 0.23 eV.

The thermodynamically most stable models have been employed to calculate the corresponding electronic band structure, density of states as well as simulated STM images. The theoretical results are in qualitatively very good agreement with the corresponding measurements. Moreover, no qualitative difference between the silicide structures formed by different rare earths could be observed or predicted.

The relative thermodynamic stability of the different phases has been investigated by *ab initio* thermodynamics. Starting from the unreconstructed, clean Si(111) surface, first the 5×2 reconstructed submonolayer structure is formed, followed by rare-earth silicide monolayers (with 1×1 periodicity) and then multilayers (with $\sqrt{3} \times \sqrt{3}$ periodicity) for increasing rare-earth exposure and therewith increasing rare-earth chemical potentials. In the experiment, on the other hand, a rather complex scenario of partly coexisting structures with different periodicities and stoichiometries as well as partially irregular domain boundaries is observed. Inhomogeneous rare-earth coverages, surface steps, kinetic limitations as well as unavoidable temperature gradients create very peculiar thermodynamic conditions locally favoring certain silicide phases. This is in particular obvious for the $2\sqrt{3} \times 2\sqrt{3}$ reconstructed structure, which is energetically less favorable than the 5×2 structure.

The combination of theoretical and experimental techniques employed here to assign structural models to the observed silicide thin films on the Si(111) surface is expected to be very helpful to investigate further silicide nanostructures on differently oriented Si substrates. On the Si(111) surface, recently a structure consisting of elongated domains with $2\sqrt{3} \times \sqrt{3}$ periodicity has been observed for multilayer rare-earth coverage, which seems to be structurally similar to the $\sqrt{3} \times \sqrt{3}$ multilayer structure reported here [74]. Also a 2×1 structure consisting of elongated islands was observed for multilayer rare-earth coverage, but its atomic structure is still unresolved [10,12,60,67]. On the Si(557) surface, which is vicinal to the Si(111) surface, the step-induced

formation of nanowires was found, consisting of RESi_2 monolayer or RE_3Si_5 multilayer stripes on the Si(111) terraces with widths of a few nanometers. On the Si(001) surface, besides the formation of strongly anisotropic 4×2 and 7×2 reconstructions, the growth of silicide nanowires is observed, which have cross sections on the nanometer scale, but lengths sometimes exceeding micrometers [13–19]. The nanowires are assumed to consist of the same hexagonal RESi_2 material as the silicide monolayers studied here. A theoretical analysis of such nanowire structures will be a fascinating task for future studies.

ACKNOWLEDGMENTS

The Deutsche Forschungsgemeinschaft (DFG) is acknowledged for the financial support by the FOR1700 research grant, projects T1 and E2. J. Große is acknowledged for assistance during the STM measurements. The authors thank M. Wanke for providing the ARPES data. All the calculations were performed at the Paderborn Center for Parallel Computing (PC^2) and at High Performance Computing Center in Stuttgart (HLRS).

-
- [1] P. Paki, U. Kafader, P. Wetzel, C. Pirri, J. C. Peruchetti, D. Bolmont, and G. Gewinner, *Phys. Rev. B* **45**, 8490 (1992).
- [2] F. A. d'Avitaya, A. Perio, J. C. Oberlin, Y. Campidelli, and J. A. Chroboczek, *Appl. Phys. Lett.* **54**, 2198 (1989).
- [3] J. A. Knapp and S. T. Picraux, *Appl. Phys. Lett.* **48**, 466 (1986).
- [4] P. Wetzel, C. Pirri, P. Paki, J. Peruchetti, D. Bolmont, and G. Gewinner, *Solid State Commun.* **82**, 235 (1992).
- [5] K. N. Tu, R. D. Thompson, and B. Y. Tsaur, *Appl. Phys. Lett.* **38**, 626 (1981).
- [6] S. Vandré, C. Preinesberger, W. Busse, and M. Dähne, *Appl. Phys. Lett.* **78**, 2012 (2001).
- [7] S. Vandré, T. Kalka, C. Preinesberger, and M. Dähne-Prietsch, *Phys. Rev. Lett.* **82**, 1927 (1999).
- [8] M. Lohmeier, W. J. Huisman, G. ter Horst, P. M. Zagwijn, E. Vlieg, C. L. Nicklin, and T. S. Turner, *Phys. Rev. B* **54**, 2004 (1996).
- [9] T. Roge, F. Palmino, C. Savall, J. Labrune, and C. Pirri, *Surf. Sci.* **383**, 350 (1997).
- [10] I. Engelhardt, C. Preinesberger, S. Becker, H. Eisele, and M. Dähne, *Surf. Sci.* **600**, 755 (2006).
- [11] C. Battaglia, H. Cercellier, C. Monney, M. G. Garnier, and P. Aebi, *Europhys. Lett.* **77**, 36003 (2007).
- [12] M. Franz, J. Große, R. Kohlhaas, and M. Dähne, *Surf. Sci.* **637-638**, 149 (2015).
- [13] C. Preinesberger, G. Pruskil, S. K. Becker, M. Dähne, D. V. Vyalikh, S. L. Molodtsov, C. Laubschat, and F. Schiller, *Appl. Phys. Lett.* **87**, 083107 (2005).
- [14] Y. Chen, D. A. A. Ohlberg, G. Medeiros-Ribeiro, Y. A. Chang, and R. S. Williams, *Appl. Phys. Lett.* **76**, 4004 (2000).
- [15] C. Preinesberger, S. K. Becker, S. Vandré, T. Kalka, and M. Dähne, *J. Appl. Phys.* **91**, 1695 (2002).
- [16] M. Wanke, K. Loser, G. Pruskil, and M. Dähne, *J. Appl. Phys.* **103**, 094319 (2008).
- [17] M. Wanke, K. Loser, G. Pruskil, and M. Dähne, *Phys. Rev. B* **79**, 155428 (2009).
- [18] M. Wanke, M. Franz, M. Vetterlein, G. Pruskil, C. Prohl, B. Höpfner, P. Stojanov, E. Huwald, J. D. Riley, and M. Dähne, *J. Appl. Phys.* **108**, 064304 (2010).
- [19] Z. He, M. Stevens, D. J. Smith, and P. A. Bennett, *Appl. Phys. Lett.* **83**, 5292 (2003).
- [20] M. Wanke, M. Franz, M. Vetterlein, G. Pruskil, B. Höpfner, C. Prohl, I. Engelhardt, P. Stojanov, E. Huwald, J. Riley, and M. Dähne, *Surf. Sci.* **603**, 2808 (2009).
- [21] L. Stauffer, A. Mharchi, C. Pirri, P. Wetzel, D. Bolmont, G. Gewinner, and C. Minot, *Phys. Rev. B* **47**, 10555 (1993).
- [22] H. Kitayama, S. Tear, D. Spence, and T. Urano, *Surf. Sci.* **482-485, Part 2**, 1481 (2001).
- [23] C. Bonet, D. Spence, and S. Tear, *Surf. Sci.* **504**, 183 (2002).
- [24] C. Rogero, C. Koitzsch, M. E. González, P. Aebi, J. Cerdá, and J. A. Martín-Gago, *Phys. Rev. B* **69**, 045312 (2004).
- [25] C. Rogero, J. A. Martín-Gago, and J. I. Cerdá, *Phys. Rev. B* **74**, 121404 (2006).
- [26] C. Koitzsch, M. Bovet, M. Garnier, P. Aebi, C. Rogero, and J. Martín-Gago, *Surf. Sci.* **566-568, Part 2**, 1047 (2004).
- [27] L. Magaud, G. Reinisch, A. Pasturel, P. Mallet, E. Dupont-Ferrier, and J.-Y. Veuille, *Europhys. Lett.* **69**, 784 (2005).
- [28] P. Wetzel, S. Saintenoy, C. Pirri, D. Bolmont, and G. Gewinner, *Phys. Rev. B* **50**, 10886 (1994).
- [29] G. H. Coccoletzi, M. R. de la Cruz, and N. Takeuchi, *Surf. Sci.* **602**, 644 (2008).
- [30] J. P. Perdew, J. A. Chevary, S. H. Vosko, K. A. Jackson, M. R. Pederson, D. J. Singh, and C. Fiolhais, *Phys. Rev. B* **46**, 6671 (1992).
- [31] J. P. Perdew, K. Burke, and M. Ernzerhof, *Phys. Rev. Lett.* **77**, 3865 (1996).
- [32] G. Kresse and J. Furthmüller, *Comput. Mater. Sci.* **6**, 15 (1996).
- [33] G. Kresse and J. Furthmüller, *Phys. Rev. B* **54**, 11169 (1996).
- [34] P. E. Blochl, *Phys. Rev. B* **50**, 17953 (1994).
- [35] G. Kresse and D. Joubert, *Phys. Rev. B* **59**, 1758 (1999).
- [36] V. I. Anisimov, F. Aryasetiawan, and A. I. Lichtenstein, *J. Phys.: Condens. Matter* **9**, 767 (1997).
- [37] S. Sanna, W. G. Schmidt, T. Frauenheim, and U. Gerstmann, *Phys. Rev. B* **80**, 104120 (2009).
- [38] S. Sanna, T. Frauenheim, and U. Gerstmann, *Phys. Rev. B* **78**, 085201 (2008).
- [39] P. Eckerlin and H. Kandler, in *Structure Data of Elements and Intermetallic Phases*, edited by K.-H. Hellwege and A. M. Hellwege, Landolt-Börnstein (Springer Materials, Berlin, Heidelberg, 1971).
- [40] E. Houssay, A. Rouault, O. Thomas, R. Madar, and J. Senateur, *Appl. Surf. Sci.* **38**, 156 (1989).
- [41] R. Wyckoff, *Crystal Structures*, 2nd ed. (Robert E. Krieger Publishing, Malabar, Florida, 1982).
- [42] H. J. Monkhorst and J. D. Pack, *Phys. Rev. B* **13**, 5188 (1976).
- [43] F. Furche, *Phys. Rev. B* **64**, 195120 (2001).
- [44] J. Neugebauer and M. Scheffler, *Phys. Rev. B* **46**, 16067 (1992).
- [45] L. Bengtsson, *Phys. Rev. B* **59**, 12301 (1999).
- [46] S. Sanna and V. Fiorentini, *Phys. Rev. B* **69**, 125208 (2004).
- [47] V. Fiorentini, *Phys. Rev. B* **46**, 2086 (1992).
- [48] J. Tersoff and D. R. Hamann, *Phys. Rev. Lett.* **50**, 1998 (1983).

- [49] J. Tersoff and D. R. Hamann, *Phys. Rev. B* **31**, 805 (1985).
- [50] H. Lin, J. Rauba, K. Thygesen, K. Jacobsen, M. Simmons, and W. Hofer, *Front. Phys. China* **5**, 369 (2010).
- [51] F. Bechstedt, *Principle of Surface Physics*, Advanced Texts in Physics (Springer, Berlin, Heidelberg, 2003).
- [52] S. Sanna and W. G. Schmidt, *Phys. Rev. B* **81**, 214116 (2010).
- [53] H. Lüth, *Surfaces and Interfaces of Solid Materials*, Springer Study Edition (Springer, Berlin, Heidelberg, 1995).
- [54] C. Rogero, C. Polop, L. Magaud, J. L. Sacedón, P. L. de Andrés, and J. A. Martín-Gago, *Phys. Rev. B* **66**, 235421 (2002).
- [55] M. Lohmeier, W. Huisman, E. Vlieg, A. Nishiyama, C. Nicklin, and T. Turner, *Surf. Sci.* **345**, 247 (1996).
- [56] P. Wetzel, C. Pirri, P. Paki, D. Bolmont, and G. Gewinner, *Phys. Rev. B* **47**, 3677 (1993).
- [57] M.-H. Tuilier, C. Pirri, D. Berling, D. Bolmont, G. Gewinner, and P. Wetzel, *Surf. Sci.* **555**, 94 (2004).
- [58] M. Franz, S. Appelfeller, C. Prohl, J. Große, H.-F. Jirschik, V. Füllert, C. Hassenstein, Z. Diemer, and M. Däne (unpublished).
- [59] R. Baptist, S. Ferrer, G. Grenet, and H. C. Poon, *Phys. Rev. Lett.* **64**, 311 (1990).
- [60] T. P. Roge, F. Palmino, C. Savall, J. C. Labrune, P. Wetzel, C. Pirri, and G. Gewinner, *Phys. Rev. B* **51**, 10998 (1995).
- [61] J. Martín-Gago, J. Gómez-Rodríguez, and J. Veullen, *Surf. Sci.* **366**, 491 (1996).
- [62] J. A. Martín-Gago, J. M. Gómez-Rodríguez, and J. Y. Veullen, *Phys. Rev. B* **55**, 5136 (1997).
- [63] P. Wetzel, S. Saintenoy, C. Pirri, D. Bolmont, G. Gewinner, T. Roge, F. Palmino, C. Savall, and J. Labrune, *Surf. Sci.* **355**, 13 (1996).
- [64] L. Magaud, A. Pasturel, G. Kresse, and J. Hafner, *Phys. Rev. B* **55**, 13479 (1997).
- [65] L. Magaud, A. Pasturel, G. Kresse, and J. Hafner, *Phys. Rev. B* **58**, 10857 (1998).
- [66] E. Perkins, I. Scott, and S. Tear, *Surf. Sci.* **578**, 80 (2005).
- [67] P. Wetzel, C. Pirri, G. Gewinner, S. Pelletier, P. Roge, F. Palmino, and J. C. Labrune, *Phys. Rev. B* **56**, 9819 (1997).
- [68] A. Kirakosian, J. McChesney, R. Bennewitz, J. Crain, J.-L. Lin, and F. Himpsel, *Surf. Sci.* **498**, L109 (2002).
- [69] M. Franz, S. Appelfeller, M. Rychetsky, and M. Dähne, *Surf. Sci.* **609**, 215 (2013).
- [70] J.-L. Li, J.-F. Jia, X.-J. Liang, X. Liu, J.-Z. Wang, Q.-K. Xue, Z.-Q. Li, J. S. Tse, Z. Zhang, and S. B. Zhang, *Phys. Rev. Lett.* **88**, 066101 (2002).
- [71] M. Y. Lai and Y. L. Wang, *Phys. Rev. B* **64**, 241404 (2001).
- [72] V. G. Kotlyar, A. V. Zotov, A. A. Saranin, T. V. Kasyanova, M. A. Cherevik, I. V. Pisarenko, and V. G. Lifshits, *Phys. Rev. B* **66**, 165401 (2002).
- [73] M. A. K. Zilani, Y. Y. Sun, H. Xu, Y. P. Feng, X.-S. Wang, and A. T. S. Wee, *Phys. Rev. B* **72**, 193402 (2005).
- [74] F. Timmer, R. Oelke, M. Franz, S. Appelfeller, M. Dähne, and J. Wollschläger (private communication, 2016).